Spectroscopic studies of the electronic structures of superconductors and topological materials

By

TIMOTHY BOYLE
DISSERTATION

Submitted in partial satisfaction of the requirements for the degree of

Doctor of Philosophy

in

Physics

in the

OFFICE OF GRADUATE STUDIES

of the

UNIVERSITY OF CALIFORNIA

DAVIS

Approved:

Eduardo H. da Silva Neto, Chair

Nicholas Curro

Valentin Taufour

Committee in Charge

2022

Abstract

This dissertation presents experimental research on the electronic structures of three crystalline materials using a combination of spectroscopic techniques. In the topological material Hf_2Te_2P, topological surface states are revealed using scanning tunneling microscopy and angle-resolved photoemission spectroscopy. The surface states exist in distinct regions of energy-momentum space and show the potential for the conductive properties of the material to be controlled via tuning of the Fermi level. In the cuprate superconductor $La_{1.475}Nd_{0.4}Sr_{0.125}CuO_4$, the effects of uniaxial stress on the strong electronic correlations are measured using resonant x-ray scattering. Uniaxial stress is shown to be a powerful tool for tuning the electronic phases of the material by causing large decreases in the onset temperatures of both the charge stripes and structural deformations. In the iron-based superconductor $FeSe_{0.77}S_{0.23}$, charge ordering is identified using scanning tunneling spectroscopy. The presence of charge order originating from orbital-selective electronic correlations provides new insight into development of superconductivity in the $FeSe_{1-x}S_x$ family. Altogether, these studies uncover new electronic properties of the materials with the goal of finding practical uses of their unique properties.

Contents

List of Figures

Acknowledgements

This research would not have been possible without help of many people.

I would like to thank my advisor, Eduardo da Silva Neto, for all of the support and guidance he has provided me with during my time in graduate school. He was a fantastic mentor and helped me foster a true appreciation for experimental condensed matter physics.

I am eternally grateful for my family, for the love and support they have given me throughout my life. Without their honesty and guidance my success in graduate school would not have been possible.

I am grateful for the close collaborative work with Morgan Walker, Santiago Blanco-Canosa, Alex Frano, Alejandro Ruiz, and Fabio Boschini. Their hands-on work in the experiments, as well as their ideas and discussions were invaluable in the conception of these projects.

I would like to thank all of the students, staff, and faculty members that helped with the success of the research at UC Davis, including Zeke Zhao, Antonio Rossi, Peter Klavins, Valentin Taufour, Nicholas Curro, Inna Vishik, Jackson Badger, and Journey Byland.

I would like to thank Ronny Sutarto and Enrico Schriele for their patience and guidance during my experiments at the synchrotron facilities.

And finally, I would like to thank Kirsty Scott and Adrian Gozar for helping me through my final years at Yale.

Chapter 1

Introduction

1.1 Symmetry, phase transitions, and topology

The concept of symmetry is integral to our understanding of nature and reality; our ability to identify shapes and patterns is key to distinguishing between different phenomena in life. In fact, different phases of matter are distinguished by their symmetry. For example, a spherical water droplet becomes a six-fold symmetric snowflake as its temperature is lowered below 0 °C, as depicted in Figure 1.1(a). While the snowflake may appear to have greater symmetry than the droplet, we say that transition results in "broken symmetry" as the appearance of the droplet is invariant to any rotation while the snowflake can only remain unchanged when rotated by multiples of 60 degrees. In general, phase transitions can be identified as changes in the number of independent parameters that define the state of a system.

While understanding the mechanics of the individual particles involved in a phase transition can be complicated, the properties of phase transitions can be expressed more simply through the concept of the order parameter - a quantity that measures the amount of symmetry breaking [1]. An illustrative example is that of a ferromagnet, where each atom possesses

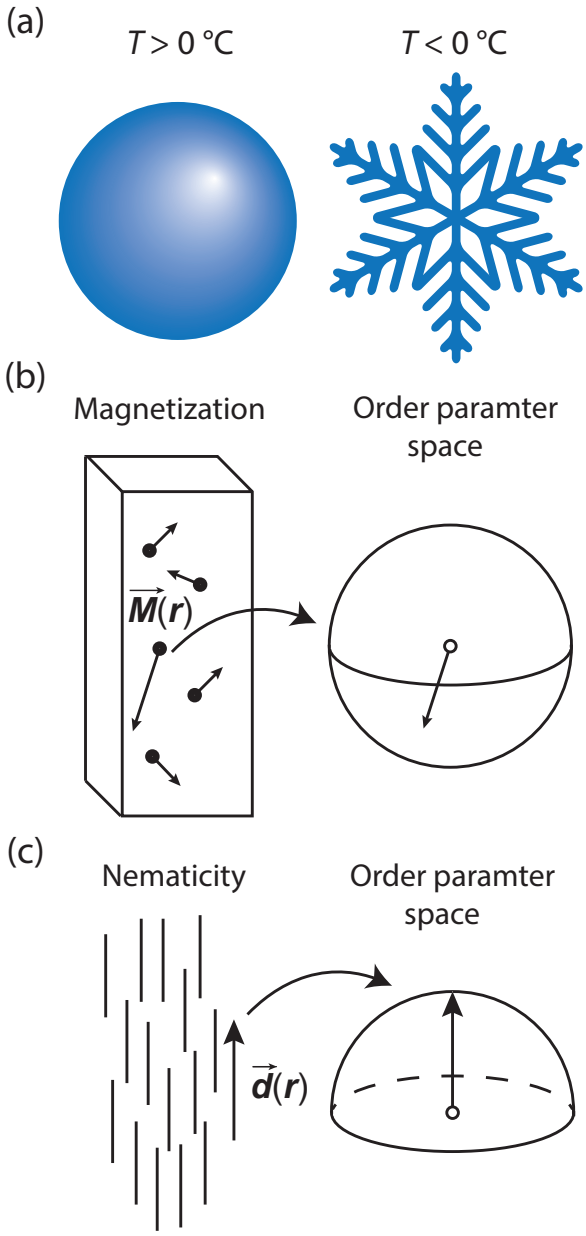

Figure 1.1: Phase transitions and order parameters: (**a**) Below $T = 0\,^{\circ}\mathrm{C}$, a spherically symmetric water droplet transitions from to six-fold symmetric snowflake. (**b**) Magnetization, $\boldsymbol{M}(\boldsymbol{r})$, is a vector that can point in any direction in 3D space, which is mapped to a sphere in order parameter space. (**c**) Nematicity is described by the director field, $\boldsymbol{d}(\boldsymbol{r})$, which is mapped to a hemisphere in order parameter space.

a magnetic moment that can point in any direction. Below a temperature known as the Curie temperature, the magnetic moments develop a preferred direction in which to point, creating magnetic domains within the system. In this case, the order parameter is defined as the magnetization, $\boldsymbol{M}(\boldsymbol{r})$ [2]. At each point $\boldsymbol{r} = (x, y, z)$ in the magnet, $\boldsymbol{M}(\boldsymbol{r})$ represents the direction and magnitude of the magnetic dipole moment per unit volume, and the entire vector field of $\boldsymbol{M}(\boldsymbol{r})$ describes the current state of the magnet. Rather than thinking of the order parameter field as a vector at each point in real space, the magnetization vectors can be projected to the origin in order-parameter space, as shown in Figure 1.1(b). Since the magnetic moments are polarized and can point in any direction in three-dimensional space, the order parameter field is mapped to a sphere.

Two examples of order-parameter spaces relevant to this thesis are those of nematic liquid crystals and superconductors. Nematic liquid crystals consist of thin, rod-like molecules that tend to align with one another. In this case, the order parameter is the director field, $\boldsymbol{d}(\boldsymbol{r})$ which points along the direction of the molecules. Since there is nothing to distinguish between the two ends of the molecules (such as the north and south poles in the case of a magnet), the parameter space is mapped to a half-sphere where opposing points on the equator represent equivalent symmetry (see Figure 1.1(c)) [3]. Superconductors, on the other hand, have a complex phase space, $\psi(\boldsymbol{r})$, that represents the complex wavefuntion of a bosonic quantum state of electron pairs. The order parameter loosely corresponds to the number of electrons that condense into the superconducting state and depends on temperature and magnetic field. Following this transition, the wavefunction develops a single phase, and the order parameter space is mapped to a circle of radius $|\psi|$. Studying the order parameter spaces of different phases is one of the keys to discovering new phases of matter and further developing our understanding of the material world.

One inherent aspect of materials is that they can contain defects, such as misaligned magnetic moments in a ferromagnet. This creates a tear or discontinuity in the order parameter space. These defects are considered topological when they cannot be patched via smooth deformations of the order parameter field. For example, a dislocation in a crystal lattice creates a distinct change in the order parameter related to the arrangement of the atoms. In this case, the defect can not be patched by rearranging the surrounding atoms and is protected from any bending or twisting of the order parameter space; this property is referred to as topological invariance. The robustness of non-trivial topological order can have direct consequences on properties of the corresponding phase, as will be discussed in the following section on topological materials.

1.2 Topological materials

Given the vast number of atoms that make up materials, crystal structures are often treated as periodic structures that extend infinitely. However, material interfaces or surfaces can have significant consequences on the properties of a material. The boundary between an insulating material and vacuous space causes an abrupt change in the band structure and can result in electronic states at the surface of the material, known as surface states. These states can arise on ideal surfaces, where the electrons can be treated using the nearly-free approximation, however surface disorder such as oxidation can easily destroy the conducting surface states.

In a three dimensional topological insulator, the surface states are protected by time-reversal symmetry, meaning that they cannot be destroyed without the application of a magnetic field. In this case, the conducting surface states continuously connect the conduction and valence bands of the bulk in the form of massless dispersions known as Dirac cones.

These Dirac fermions have spin-momentum locking such that the $\boldsymbol{k}$ and $-\boldsymbol{k}$ states have opposite spins. The consequence of this spin independence is topological protection from backscattering, creating a material phase with an insulating bulk and robust conducting surface states that are protected against surface disorder such as defects and impurities [4].

Furthermore, Kane et al. showed that topological insulators (TIs) are associated with a $\mathbb{Z}_2$ topological invariant, which identifies the number of times an edge state crosses the Fermi level in the first Brillioun zone [5]. In three dimensions, the $\mathbb{Z}_2$ invariant differentiates strong and weak TIs. Weak TIs are effectively stacks of 2D TIs with edge states, thus they only conduct on some surfaces. Strong TIs, on the other hand, conduct on all surfaces. Materials can feature multiple surface states with different topological order in distinct regions of energy-momentum space, such as Hf_2Te_2P. These materials can provide avenues to realize new technologies such as switchable electronic devices and dissipationless transistors [6]. Chapter 2 presents a study of the topological surface states in Hf_2Te_2P using a combination of spectroscopic techniques [7].

1.3 Superconductors

Materials exhibit two properties when entering the superconducting phase: the interior magnetic field is spontaneously expelled and the electrical resistance goes to zero. Superconductors have the potential to completely revolutionize technology and infrastructure by greatly reducing the energy loss of power transmission. Dissipationless transport is not exclusive to superconductors as it can also been found in the conducting surface states of a topological insulator. However, superconductors exhibit dissipationless transport in the bulk and perfect diamagnetism, which can provide additional applications such as magnetic levitation. Despite their promising applications, superconductors are relatively absent in everyday life

due to the exceedingly low temperatures at which superconductivity occurs. Nonetheless, superconductivity has been an active topic of research for over a century with the prospect of achieving room-temperature superconductivity.

The dissipationless transport of conventional superconductors can be attributed to the formation of electron pairs, also referred to as Cooper pairs, which form via a phonon-mediated weak electron-electron attraction [8]. While this theory has proven useful in describing the superconductivity of some simple metals such as Sn, it fails in describing the mechanisms of superconductivity in many of the modern, higher critical-temperature materials, leading these materials to be dubbed 'unconventional' [9].

The Cooper pairs in unconventional superconductors are not bound together by a phonon interaction. Instead, superconductivity is thought to emerge from charge and spin fluctuations, mainly antiferromagnetism and charge ordering [10]. In fact, unconventional superconductors often host a multitude of phases that interact with superconductivity and develop with parameters such as temperature, magnetic field, and chemical-doping. Studying the interactions between the intertwined orders and superconductivity has provided significant insight into the pairing mechanisms of unconventional superconductors and has unveiled a plethora of unique physical phenomena. This dissertation focuses on the electronic ordering in two unconventional superconductors: $La_{1.475}Nd_{0.4}Sr_{0.125}CuO_4$, a copper-oxide (cuprate) material, and $FeSe_{1-x}S_x$, an iron-based superconductor (IBSC).

1.3.1 Charge order in the cuprates and iron-based superconductors

The cuprates are a family of superconducting materials containing layered crystal structures with square planes of CuO_2. The synthesis of different cuprate materials has provided many

breakthroughs in the field of superconductivity, including the first material to reach a T_c above the temperature of liquid nitrogen with the discovery of a Y-Ba-Cu-O compound in 1987 [11], and the material with the current highest transition temperature $T_c = 133\,\mathrm{K}$ at ambient pressure with the discovery of an Hg-Ba-Ca-Cu-O system in 1993 [12]. The copper oxide layers host the superconductivity in addition to various magnetic and charge ordering states. These layers can effectively be thought of as charge reservoirs, where electrons can be added and removed via electron and hole doping. In their normal state, cuprates are Mott insulators with antiferromagnetic ordering. However, with hole doping, several electronic properties emerge including superconductivity, charge ordering and Fermi surface reconstruction.

Charge order (CO) refers to various phases that exhibit symmetry breaking charge patterns that are incommensurate with the crystal lattice, such as short- or long-range charge density waves. CO has been shown to interact strongly with superconductivity, with many phases exhibiting competing effects [13–15]. In $La_{1.475}Nd_{0.4}Sr_{0.125}CuO_4$, superconductivity emerges as a function of hole-doping around $x = 0.05$ and reaches a maximum critical temperature of 15 K at $x \approx 0.18$ [16, 17]. Around $x = 0.1$, CO appears in the form of charge stripes that compete with superconductivity, causing T_c to decrease as the charge stripes form. The strong interactions between the charge density wave and T_c may provide key insights into the superconducting pairing mechanism in this material. In Chapter 3, a study of the interactions between the intertwined phases in $La_{1.475}Nd_{0.4}Sr_{0.125}CuO_4$ and uniaxial stress is presented, providing new insight into the complex relationship between CO and superconductivity in the cuprates [18].

The iron-based superconductors (IBSCs) are another family of unconventional superconductors with rich phase diagrams of interacting orders. In a similar fashion to the cuprates, most of the materials exhibit an antiferromagnetic ground state that develops into super-

conductivity with chemical doping. Additionally, they host strong electron correlations, electronic nematicity, and orbital selectivity. Despite the presence of strong electronic correlations, CO has yet to be observed in an IBSC. Chapter 4 presents the first observation of CO in an IBSC using scanning tunneling spectroscopy. This CO appears outside of the electronic nematic state and likely emerges from the orbital selective correlations. As with the cuprates, understanding the interactions between the CO and superconducitivity may provide insight into the symmetry of the superconducting order parameter and pairing mechanism in these materials.

1.4 Instrumentation

The experimental work presented uses a combination of spectroscopic techniques to study the energy-dependent electronic structures of the materials. Spectroscopy typically refers to the study of the interactions between electromagnetic radiation and matter, however it also includes experiments that measure energy dependent features of a material without the use of light. The techniques used here include scanning tunneling microscopy/spectroscopy (STM/S) and synchrotron-based scattering and photoemission techniques.

1.4.1 Scanning tunneling microscopy

The STM was invented in 1981 by IBM researchers Gerd Binning and Heinrich Rohrer [19]. Likened to the impact of the discovery of the telescope to astronomy, the STM has had a profound impact on material science. While initially seen as a high-resolution probe for surface topology, the STM has been used in a wide variety of experiments and applications, including single atom manipulation and in the investigation of the vibrational, electronic, and magnetic properties of materials [20].

An STM operates by bringing an atomically-sharp metallic tip a few angstroms away from a flat surface of a material. A bias voltage is applied to the sample while the tip is grounded, which generates a relative shift of their Fermi levels [21]. This causes a tunneling current to flow between the tip and sample that depends on the density of states (DOS) of both the tip, $\rho_t(E)$, and sample, $\rho_s(E)$. For a metallic tip, the current flow will only depend on ρ_s and a matrix element, $|M|^2$, and can be approximated for a given bias voltage, V, as

$$I(V) = \frac{4\pi e}{\hbar}|M|^2\rho_t(0)\int_0^{eV}\rho_s(E)\,dE. \tag{1.1}$$

This is the basic operating principle of an STM, which says that the tunneling current is proportional to the integral of the density of states of the sample from 0 to eV. The matrix element depends on the details of the junction and tunneling barrier, such as the shape of the tip and the sample's work function. Importantly, $|M|^2$ has an inverse exponential dependence on the tip-sample distance. In other words, the tunneling current increases exponentially as the tip is brought closer to the sample.

Using piezoelectric actuators, the position of tip can be controlled with sub-nanometer precision. As the tip is scanned across a flat surface, the current can be recorded and will vary according the local DOS. Given that electrons in a material are concentrated around atoms, one can perform this type of measurement to measure the atomic lattice of the material. While operating in this mode is certainly possible, it is not practical given (1) the susceptibility of the instrument to external vibrations and (2) possible variations in the surface of the sample. These issues can be mitigated by experimental procedures, such as suspending the instrument from springs to dampen vibrations from the environment and cleaving the sample to expose a clean surface. However, they can be avoided by imposing a feedback loop to regulate the height of the tip. This is done using a negative feedback

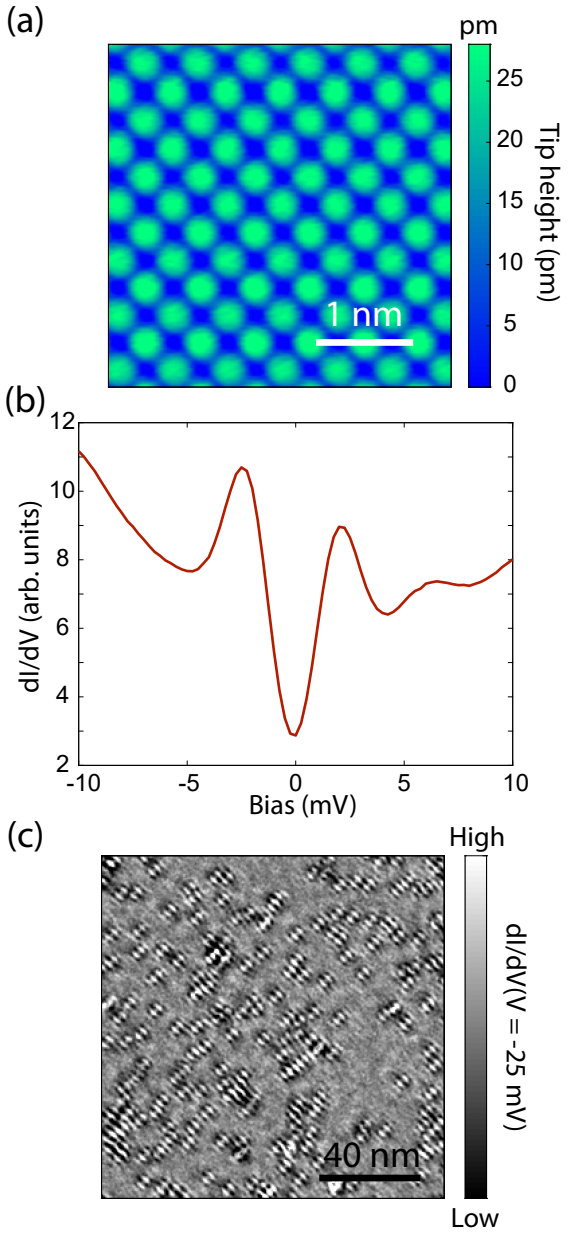

Figure 1.2: STM measurements: (**a**) Constant current topography of the surface FeSe, displaying square lattice of Se atoms. (**b**) Differential conductance of FeSe at $T = 4.2\,K$. (**c**) dI/dV map on the surface of FeSe showing a quasiparticle interfence pattern.

loop via a proportional–integral–derivative controller, which adjusts the height of the tip to maintain a constant tunneling current according to the user defined setpoint value. Following this procedure, as the tip scans and encounters areas of high density of states or a feature of the surface that changes the distance between the tip and the sample, the controller will withdraw the tip to decrease the current back to the setpoint value. This procedure effectively regulates the tip-sample distance to correct for noise and surface features. The height of the tip can then be recorded as a function of the position across the sample which creates as a topographic image of the surface accounting for both the DOS of the sample and surface structure. This type of measurement is shown in Figure 1.2(a) on the surface of a FeSe crystal.

In addition to topographies, STMs are capable of spectroscopic measurements by measuring the DOS of a material as a function of energy. This measurement is done without a feedback loop, and instead the tip is held at a fixed position above the sample. A sinusoidal modulation is applied to the bias voltage and a lock-in amplifier is used to record the differential conductance, $dI/dV(V)$. We can solve for $dI/dV(V)$ by taking the derivative of Equation 1.1:

$$\frac{dI}{dV}(V) = \frac{4\pi e}{\hbar}|M|^2\rho_t(0)\rho_s(eV). \tag{1.2}$$

From this equation, we see that the differential conductance is directly proportional to the DOS of the sample at the energy $E = eV$. By measuring dI/dV for a set of bias volages, one can measure the local DOS directly, as shown in Figure 1.2(b).

Scanning the tip and recording dI/dV across the surface of the sample is a powerful spectroscopic tool allowing for high-resolution measurements of the local density of states as a function of energy. One important property that can be measured using STS is the interference pattern of quasiparticles. Quasi-particle interference (QPI) is the interference

between the wave functions of electrons, $\psi(x)$, as they scatter off of defects within the crystal. Figure 1.2(c) shows a dI/dV map on the surface of FeSe at $V = -25\,\mathrm{mV}$, revealing quasiparticle interference patterns emanating from iron-vacancies in the crystal.

In general, QPI scattering events can be expected to occur between highly occupied momentum states, i.e. areas with a high joint DOS. The wavelength of the modulations is determined by the momentum of the electrons at the energy of the bias voltage. This is represented as a scattering vector in momentum space, $\boldsymbol{Q}(E) = \boldsymbol{k}_f(E) - \boldsymbol{k}_i(E)$, which can be computed from the Fourier transform of the real-space DOS. This quantity represents the period of the interference pattern of the electron wavefunctions, however it only contains information about the momentum transfer, $\boldsymbol{Q}(E)$, and not states of the electrons themselves. The momentum states, $\boldsymbol{k}_f(E)$ and $\boldsymbol{k}_i(E)$, are determined by the band structure of the material. Prior knowledge of the electronic band structure of the material, such as from angle resolved photoemission spectroscopy (ARPES) or density-fuctional theory, is needed to determine the origin of the scattering event and the specific momentum states that are involved.

ARPES measures a material's density of states below the Fermi level with momentum resolution and complements QPI data by providing direct access to the band structure. The technique utilizes the photoelectric effect where monochromatic light is incident upon a single, flat surface of a material, causing electrons to eject from the surface. These electrons contain information about the energy and momentum states inside of the material. By manipulating their trajectories using a magnetic field, the electronic band structure can be resolved up to the highest occupation level, i.e. the Fermi level. The scattering vectors obtained from QPI can then be compared with the band structure obtained from ARPES to determine their exact location in momentum-space. One advantage of STS over ARPES is that it is capable of measuring both the occupied and unoccupied states of the band

structure. However, when combined, STS and ARPES can provide detailed information about the band structure of materials.

1.4.2 Resonant x-ray scattering

Resonant x-ray scattering (RXS) measures diffraction patterns of crystals using high-intensity monochromatic light with the photon energy tuned to an x-ray absorption edge. The incoming photons interact with the electrons in the system and the scattered rays provide information about the relative positions, energy, and spin of the electrons. The process can be described theoretically by treating the light-matter interaction Hamiltonian as a perturbation to the system [22]:

$$H = \sum_j \frac{1}{2m_e} \left(\boldsymbol{p}_j - \frac{e}{c} \boldsymbol{A}(\boldsymbol{r}_j, t) \right)^2 . \tag{1.3}$$

This introduces two terms that are linear and quadratic in the vector potential, $\boldsymbol{A}$. Following Fermi's golden rule, the first- and second order transition probabilities can be derived, which determine the flux of the scattered photons for a given scattering vector, $\boldsymbol{Q}$, and photon energy, $\hbar\omega$:

$$\omega_1 \propto | \langle \psi_{GS} | \, \rho(\boldsymbol{Q}) \, | \psi_{GS} \rangle \, |^2 \tag{1.4}$$

$$\omega_2 \propto \left| \sum_m \sum_{j,k} \frac{\langle \psi_{GS} | \, \epsilon_{\nu_{in}} \cdot \boldsymbol{p}_j \cdot e^{i\boldsymbol{q}_{in} \cdot \boldsymbol{r}_j} \, | \psi_m \rangle \, \langle \psi_m | \, \epsilon_{\nu_{out}} \cdot \boldsymbol{p}_k \cdot e^{-i\boldsymbol{q}_{out} \cdot \boldsymbol{r}_k} \, | \psi_{GS} \rangle}{\epsilon_{GS} - \epsilon_m + \hbar\omega + i\Gamma_m} \right|^2 \tag{1.5}$$

The first order term, ω_1, corresponds to Thomson scattering and measures the reciprocal space lattice of the crystal. The second order term, ω_2, describes the resonance process, which involves the absorption and emmission of a photon. An electron in its ground state,

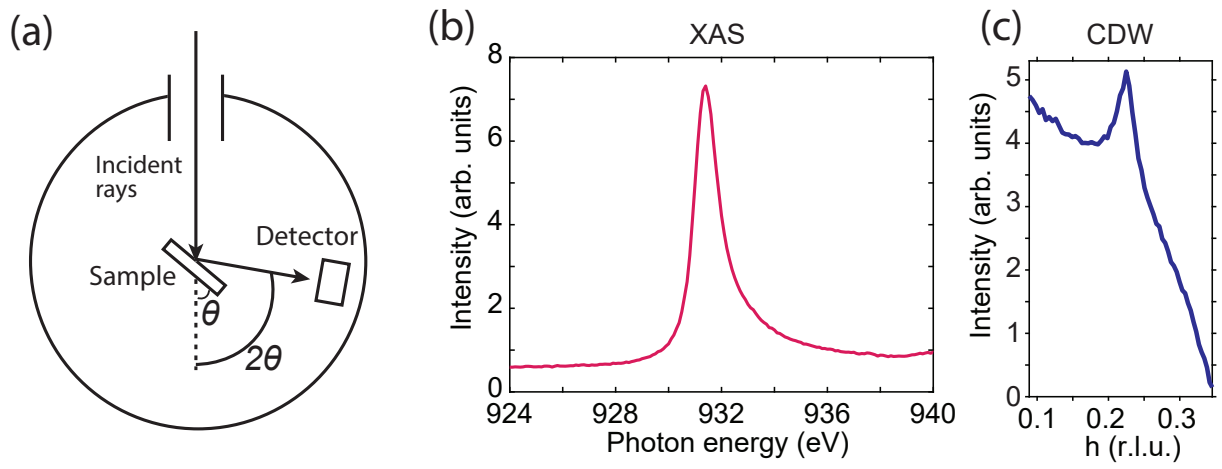

Figure 1.3: RXS measurements: (**a**) RXS endstation. The incident rays enter the chamber at a fixed position with variable photon energy. The sample and detector are rotated to measure different points in reicprocal space. (**b**) An XAS measurement at the Cu-L_3 edge. (**c**) A CDW measuremnt on $La_{1.475}Nd_{0.4}Sr_{0.125}CuO_4$.

ψ_{GS}, absorbs a photon and is promoted to an intermediate state, ψ_m. Subsequently, the electron returns to its ground state by emitting a photon. When the photon energy is tuned the difference between the intermediate and ground state energies (i.e. an x-ray absorption edge), $\hbar\omega = \epsilon_m - \epsilon_{GS}$, the magnitude of the transition probability increases, creating a large enhancement of the outgoing photon flux.

RXS experiments are performed at synchrotron facilities, which provide high-intensity, broad spectrum electromagnetic radiation by accelerating electrons to nearly the speed of light. The radiation then passes to an optics hutch, where a monochromator isolates the specific photon energy. A series of mirrors focuses the beam into the endstation, which contains the diffractometer and detectors. A diagram of a typical RXS endstation is shown in Figure 1.3(a). Light enters the chamber at a fixed position while the angles of the sample, θ, and detector, 2θ, are variable.

For measurements of charge density waves, the photon energy of the incident rays is tuned to the absorption edge of the valence electrons. In the case of the cuprates and the iron-based superconductors, this corresponds to the Cu- and Fe-L_3 edges. An x-ray absorption spectroscopy measurement on $La_{1.475}Nd_{0.4}Sr_{0.125}CuO_4$ is shown in Figure 1.3(b). The peak at $E \approx 932\,\text{eV}$ is a result of the resonant enhancement at the Cu-L_3 edge. With the photon energy set, CDW measurements are carried out by rocking the sample within the scattering plane to measure the outgoing intensity as a function of a position vector in reciprocal space, $\boldsymbol{Q}(h, r, l) = \boldsymbol{k}_f - \boldsymbol{k}_i$, where h, k, and l follow Miller index notation (see Appendix B for more detailed information on scattering geometry). Figure 1.3(c) shows a RXS CO scan, which was performed by rotating θ and measuring the outgoing intensity at a fixed detector angle with the photon energy tuned to the Cu-L_3 edge. The scan shows a peak at $Q = 0.23\,(\text{r.l.u.})$ in $La_{1.475}Nd_{0.4}Sr_{0.125}CuO_4$, corresponding to a CDW with a wavelength of approximately four times the lattice constant. The peak position and width correspond to the period and correlation length of the CO. Combined with cryogenic temperatures and high-magnetic fields, RXS is a powerful tool for characterizing the different properties of CO.

Chapter 2

STS and ARPES reveal topological surface states in Hf_2Te_2P

This project began in 2018 as a collaborative effort between three condensed matter experiment groups at UC Davis. Valentin Taufour's group synthesized the crystals, Eduardo da Silva Neto's group performed the STS measurements, and Inna Vishik's group performed the ARPES experiments. The results were published in 2019 as a Rapid Communication in Physical Review B [7].

2.1 Introduction

Topological quantum phases have been discovered in a variety of materials such as topological insulators, Dirac and Weyl semimetals, and nodal line semimetals [6, 23–26]. All of these topological phases result in non-trivial topological surface states (SSs), which could be used for future low-dissipation electronic or spintronic technologies [24, 27, 28]. Although several materials that host one of the aforementioned topological phases have been discovered,

quantum materials that exhibit several SSs at distinct regions of energy-momentum space are not common. Two materials that exhibit mutliple SSs are Zr_2Te_2P [29] and. Hf_2Te_2P [30]. Band structure calculations and experiments indicate a rich phenomenology of topological electronic states in these systems, including multiple SSs. In particular, for Hf_2Te_2P, the calculations find four SSs as follows, where the energies are relative to the Fermi level (E_F): three dispersions at the Γ point near 0.46 eV (SS1), 0.17 eV (SS2), -1.2 eV (SS3), and a Dirac node-arc along the Γ-M direction, centered at the M-point near -0.9 eV (SS4). Similar features (SS1, SS2 and SS4) were also predicted in Zr_2Te_2P. This unusual multitude of states in a single material stems from the topological character of various bulk bands originating from Te-p and Hf-d orbitals. Following Fu and Kane [31], the four topological $\mathbb{Z}_2$ invariants were computed from the calculated band structure. From this analysis, SS4 at -0.9 eV was identified to have a weak topological $\mathbb{Z}_2$ invariant, while SS1 at 0.46 eV yields a strong $\mathbb{Z}_2$ invariant. The topological nature of SS2 and SS3 could not be clearly resolved, with SS2 displaying a significant bulk-surface mixing [30].

Among the SSs in Hf_2Te_2P, SS1 at 0.46 eV may be the one with the greatest potential toward future applications for several reasons. First, excluding SS2 due to its surface-bulk mixing, SS1 is the closest state to the Fermi level of Hf_2Te_2P. Second, it is the only SS centered within a clear direct gap in the bulk. Third, its topological nature originates from the inversion of Te-p and Hf-d orbitals, which could lead to a better surface to bulk conduction ratio when compared to more traditional topological insulators like Bi_2Te_3 or Bi_2Se_3, where only p-orbitals are involved [29, 30, 32]. This favourable surface conduction stems from the more localized nature of the Hf-d (or Zr-d in the case of Zr_2Te_2P) states, leading to a higher effective mass for the bulk electrons when compared to Bi_2Te_3 or Bi_2Se_3, or even to the other SSs in Hf_2Te_2P that do not involve Hf-d orbitals. Additionally, this

would render the interesting combination of topology and strong electron correlations, if E_F is tuned to within the pseudogap.

Experimentally, the SSs in Zr_2Te_2P and Hf_2Te_2P below the Fermi level, E_F, have been resolved through angle-resolved photo-emission spectroscopy (ARPES) measurements, showing a remarkable agreement to the band structure predictions [29, 30]. However, since ARPES experiments are not able to probe the SS1 state above the Fermi level, this key topological state still lacks direct experimental evidence.

In this work, two methods are used to experimentally access the states above E_F and provide the direct evidence for SS1 in Hf_2Te_2P. First, through the deposition of K-atoms the surface of the material becomes electron-doped, enabling ARPES to measure states up to approximately 160 meV above the original E_F. Second, scanning tunneling microscopy and spectroscopy (STM/S) is used to measure energy-resolved quasiparticle interference (QPI) patterns on the surface of Hf_2Te_2P, which allows us to probe the energy-momentum structure both above and below E_F [4, 33–39]. Using the combined ARPES and STM/S data, and their comparison to the reported surface band structure calculations, the SSs of Hf_2Te_2P above E_F are resolved revealing Dirac-like dispersive bands centered at 170 meV and 460 meV, where the SS1 and SS2 states have been predicted.

2.2 Methods

2.2.1 Crystal Synthesis

The synthesis was perfomed by Peter Carlson, Moira Miller, Jing-Tai Zhao, Peter Klavins, and Valentin Taufour. Single crystals of Hf_2Te_2P were grown from vapor transport following the synthesis developed for the isostructural Zr_2Te_2P [40], also detailed in Ref.[41]. Stoi-

chiometric amounts of Hf powder (Alfa Aesar, 325 mesh, 2N6), Te pieces (Alfa Aesar, 5N) and P pieces (JMC, 6N5) were sealed under vacuum in a silica tube, heated to 1000 °C in 15 hours, held at 1000 °C for 24 hours, after which the furnace was turned off and allowed to cool down. The polycrystalline sample was resealed with iodine (1.3 g of Hf_2Te_2P and 46 mg of iodine) in a silica tube approximatively 10 cm long, 14 mm inner diameter. The tube was heated in a two-zone furnace with a hot zone at 900 °C and a cold zone at 800 °C. The furnace was turned off after two weeks. The precursor powder was in the cold zone, and the crystals formed near the hot zone, as reported previously [40].

2.2.2 STM/S

STM/S measurements were done by Morgan Walker, Eduardo da Silva Neto, and myself using a customized Unisoku USM-1300 instrument using a W tip. The samples were cleaved *in situ* in an ultra-high vacuum (UHV) environment with pressures below 1×10^{-9} Torr. All STM/S measurements were performed at 4.2 K. For the differential conductance maps, a modulation amplitude of 10 was used and the bias and current setpoints were 800 mV and 500 pA respectively. Data were collected over a 256 x 256 spatial grid. The single crystals of Hf_2Te_2P were grown from vapor transport following the synthesis developed for the isostructural Zr_2Te_2P [40], also detailed in Ref. [41].

Distinct high and low points recur in the real-space STS differential conductance maps. These features appear independently of energy and are due to the underlying inhomogeneity of the cleaved surfaces. This is evident from the juxtaposition of a dI/dV map Fig. 2.1(a) a topography Fig. 2.1(b) simultaneously acquired over the same spatial region, with the dI/dV map taken at 460 meV. The topography contains both a speckled pattern of high intensity points and small circular depressions. The speckled pattern is shown more clearly

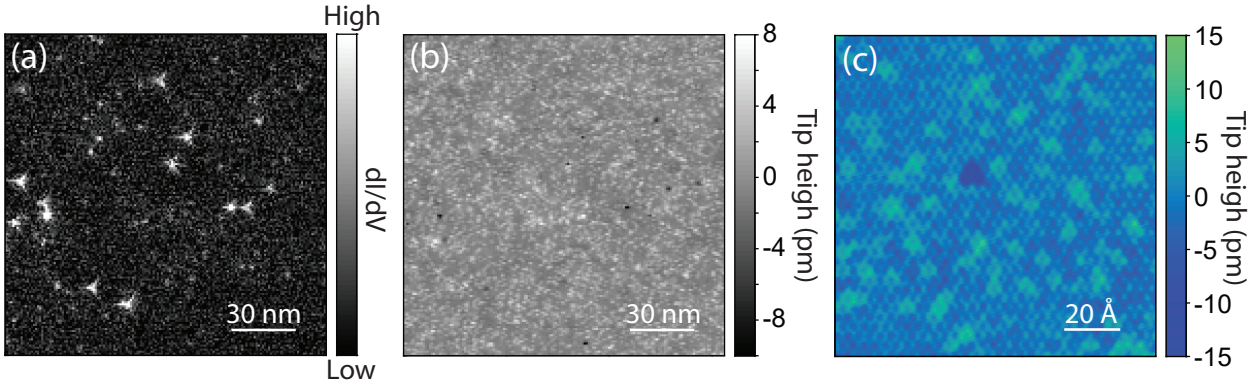

Figure 2.1: Surface inhomogeneity: (**a**) STS measured differential conductance map taken at 460 meV. The bright spots correspond to surface defects. (**b**) Constant-current topography taken over the same region of space as (a) with a current setpoint of 500 pA and 800 mV sample bias. Here the defects show up as small deppressions. (**c**) Constant-current topography with a current setpoint of 3 nA and -70 mV sample bias, showing surface inhomogeneity and a defect.

in the topographic image in Fig. 2.1(c), where green blotches are spread across the surface. Another single defect is also visible in this topography in the form of a small triangular depression. Comparing Figs. 2.1 (a) and (b), the speckled pattern can be seen in both images. Note that the depressions in the topography (b) coincide with the strong peaks in the dI/dV maps (a). Overall, there is a strong correspondence between the spatial patterns in (a) and (b), as reflected in their normalized cross-correlation, which was calculated to be -0.66. Note that the strong peaks in (a) were cut off from the data displayed in the main text, to allow the QPI patterns to be clearly observed in the figures.

Measurements of QPI patterns require scattering centers (e.g. point defects), which inevitably result in non-QPI variations of the LDOS. It may be easy to disentangle both signals if they have dissimilar characteristic wavelengths, which often happens but is not the case in Hf_2Te_2P. Because the topological surface states of interest have a relatively high velocity, the intra-pocket scattering signal from the bands results in large wavelength QPI – which is also why the measurements were taken over a large field-of-view ($120 \times 120\,\mathrm{nm}^2$).

The Q-space measurements shown feature and strong central peak due to the inhomogeneity of the sample surface, as seen in Fig. 2.2(a). Although dispersing bands can still be observed, the presence of the central-peak hinders their visualization. To overcome this, the second derivative of the data with respect to Q is taken, Fig. 2.2(a), which accentuates the peak features by eliminating linear backgrounds. This technique, however, can deceptively give prominence to small features in the absence of strong peaks. Such is the case for maps taken at energies at which small scattering signals are observed. For these energies (e.g. 460 and 210 meV), "tail-like" features are observed over relatively wide ranges of Q frequencies after taking the second derivative (see Fig. 2.2(c)). Notice that the normalized "raw" Q-vector band dispersion in Fig. 2.2(b) does not show strong spectral weight in the regions where the tails appear. Furthermore, the Q-distribution curves (QDCs) show the lack of dispersive features in these regions.

2.2.3 ARPES

ARPES experiments were performed by Antonio Rossi and myself with the assistance of Aaron Bostwick, Eli Rotenberg, and Chris Jozwiak at beamline 7.0.2 MAESTRO at the Advanced Light Source. The μ-ARPES endstation allows for a spot size of 80 μm x 80 μm, which is crucial to scanning a homogeneous region in a cleaved area. After growth, the Hf_2Te_2P crystals were sealed in an inert environment, transferred into a glove box at the beamline and cleaved. From the glove box, they were transferred into the UHV ARPES chamber without air exposure and cleaved a second time *in situ*.

The measurements were done at 77 K with a photon energy of 100 eV, using horizontally linearly polarized photons and 120 meV energy resolution. The Fermi level was determined by fitting the edge of the momentum integrated energy distribution curves to the convolution

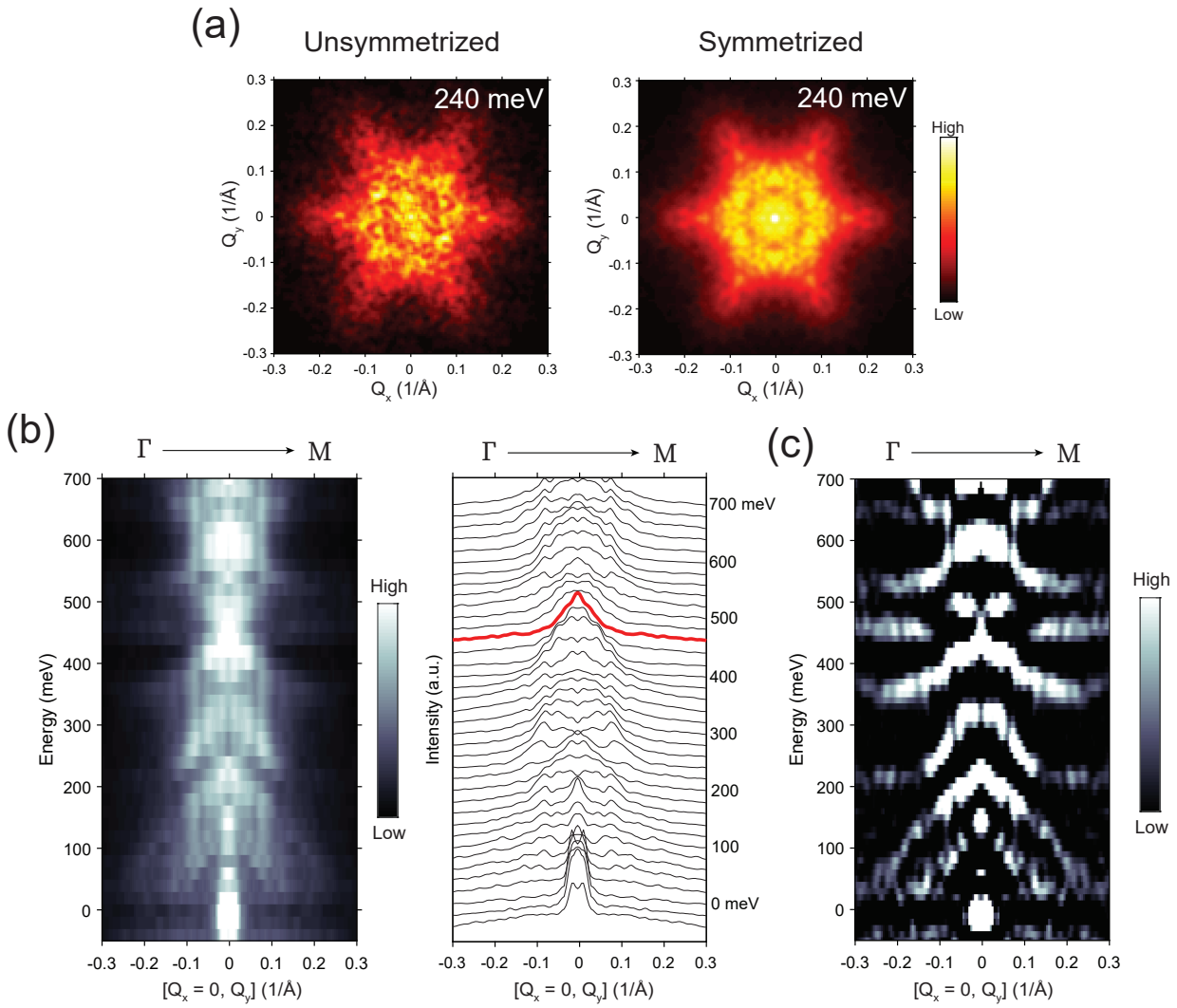

Figure 2.2: STS analysis: (**a**) Unsymmetrized versions of the Fourier transformed QPI data. (**b**) Normalized Q-vector band dispersions (left) and QDCs (right). The curve at $E = 460\,\text{meV}$ is highlighted in red. (**c**) The second derivative of the Q-vector band dispersions along Γ-M and Γ-K.

of a Gaussian and a Fermi-Dirac function; the Fermi level is set by the position of the Fermi-Dirac function and the full-width at half-maximum of the Gaussian determines the energy resolution (see Fig. 2.3(d)).

The sample surface was doped with K using a commercial SAES alkali metal dispenser. K-doping promotes the occupation of states above the Fermi level of the undoped sample, which increases the Fermi energy. To clearly convey this effect, the K-doped band dispersion are plotted such that 0 meV represents the Fermi level of the undoped sample. To determine the relative energy shift achieved by doping, the band structures were compared visually and adjusted to maximize their overlapping. Conservatively, the uncertainty in the alignment is ± 35 meV. Fig. 2.3(a) shows a wide view of the Fermi surface with well defined contours. The band structure, shown in Fig. 2.3(b), contains very sharp bands, which is also evident from the distinct peaks in the momentum distribution curves shown in Fig. 2.2(c). These data sets attest to the high quality samples used for these experiments.

2.3 Results

Figure 2.4(a) shows the crystal structure of Hf_2Te_2P, where the atoms between consecutive Te layers along the c-axis are bonded by weak Van der Waals forces. This makes the Te layer the most likely termination resulting from the cleaving process [30]. Figure 2.4(b) shows an atomically resolved STM constant-current topography on a cleaved surface of Hf_2Te_2P, featuring a hexagonal structure with lattice constants that are consistent with those obtained from x-ray diffraction [41]. Localized defects are observed, appearing as depressions in the topography, as well as smoother features which may reflect underlying defects. After scanning multiple crystals, only the Te-termination was observed in the STM measurements. Using the same *in situ* cleaving process, the ARPES measurements yield the occupied electronic

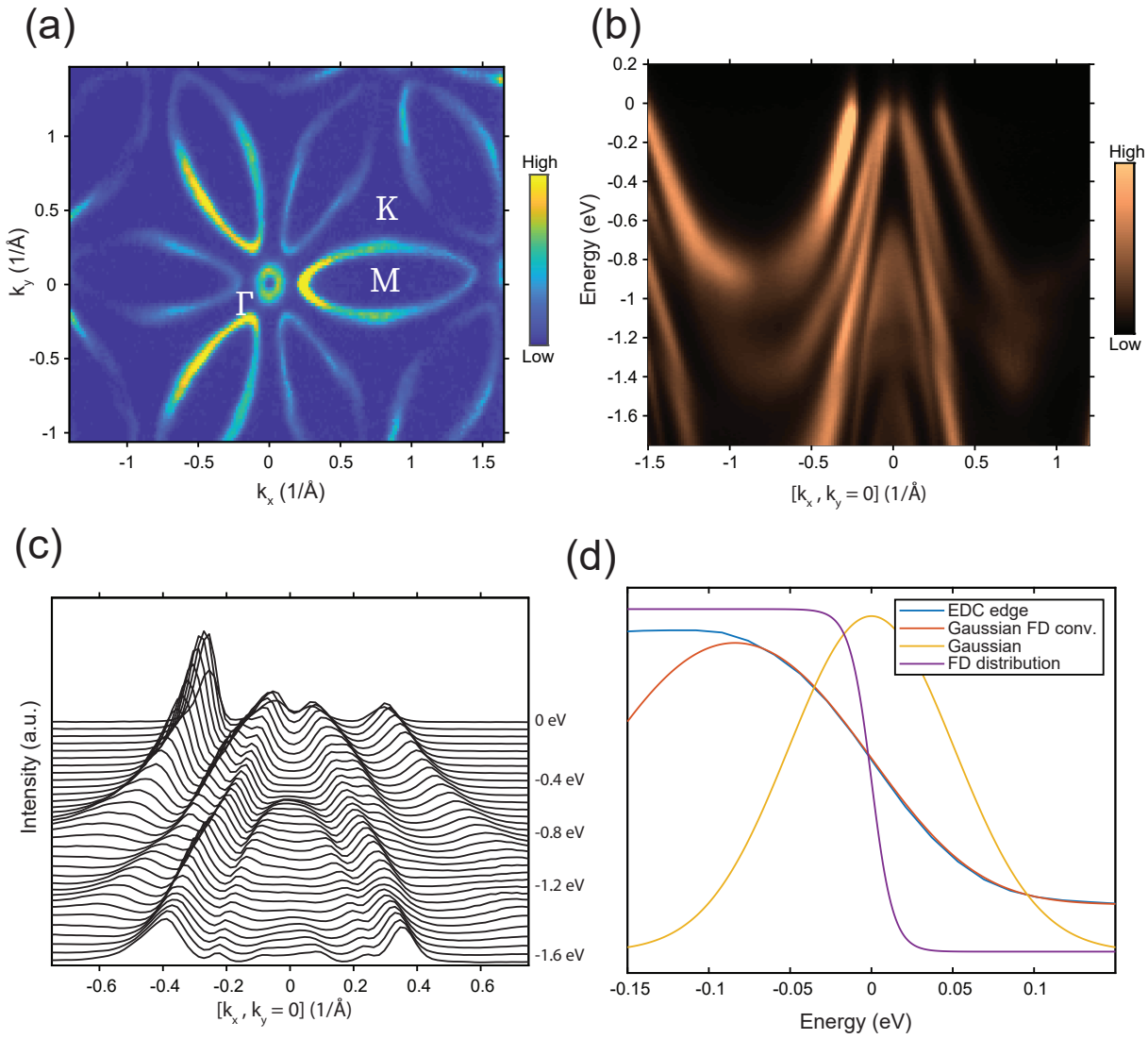

Figure 2.3: Undoped ARPES measurements on pristine sample: (**a**) ARPES measured Fermi surface of a pristine sample. (**b**) Band structure along Γ-M. (**c**) Momentum distribution curves along Γ-M. (**d**) A graph showing how the Fermi level was determined for the undoped data. The edge of a momentum-integrated EDC was fit to the convolution of a Gaussian and Fermi-Dirac function.

structure of Hf_2Te_2P. Figure 2.4(c) displays the result of the ARPES measured Fermi surface, which shows a hole-like pocket centered at the Γ point and electron-like flower patterns, consistent with previous measurements. Overall, the momentum distribution curves (MDCs) show extremely sharp features which, together with the atomic resolution obtained in STM measurements, indicate the high quality of the surfaces obtained from the cleaving process. Figure 2.4(d) shows a representative measurement of the differential conductance, dI/dV, which is proportional to the density of states as a function of energy. The most prominent feature in the spectrum is a pseudogap centered around 500 mV, with a small but non-zero density of states that could have surface and/or bulk origin.

2.3.1 SS1

SS1 is predicted near 170 meV at the Γ point [30]. To access states above E_F with ARPES, K-atoms were deposited on the cleaved surface of Hf_2Te_2P, which occupy the states above E_F and enables their photo-emission [42]. Figures 2.5(a-e) show the evolution of the constant energy contours for positive energies where zero refers to the Fermi level of the sample before K-doping. The data in Fig. 2.5(a-e) indicate the collapse of the hole pocket into a single point at Γ, which is more clearly observed in the dispersion plot through $k_y = 0$, Fig. 2.5(g), and could not be resolved without the K-doping – compare to data in Fig. 2.5(f), prior to K-doping.

The presence of the surface state at 170 meV is confirmed via STS measurements of QPI patterns. Figures 2.6(a-c) show dI/dV maps for different energies above E_F over a large field-of-view, 120 nm × 120 nm. The maps were taken by measuring dI/dV while performing bias sweeps from 700 meV to −100 meV with 20 meV steps on a 256 × 256 spatial grid. It is evident from the STS maps that the characteristic length scales of the modulations in

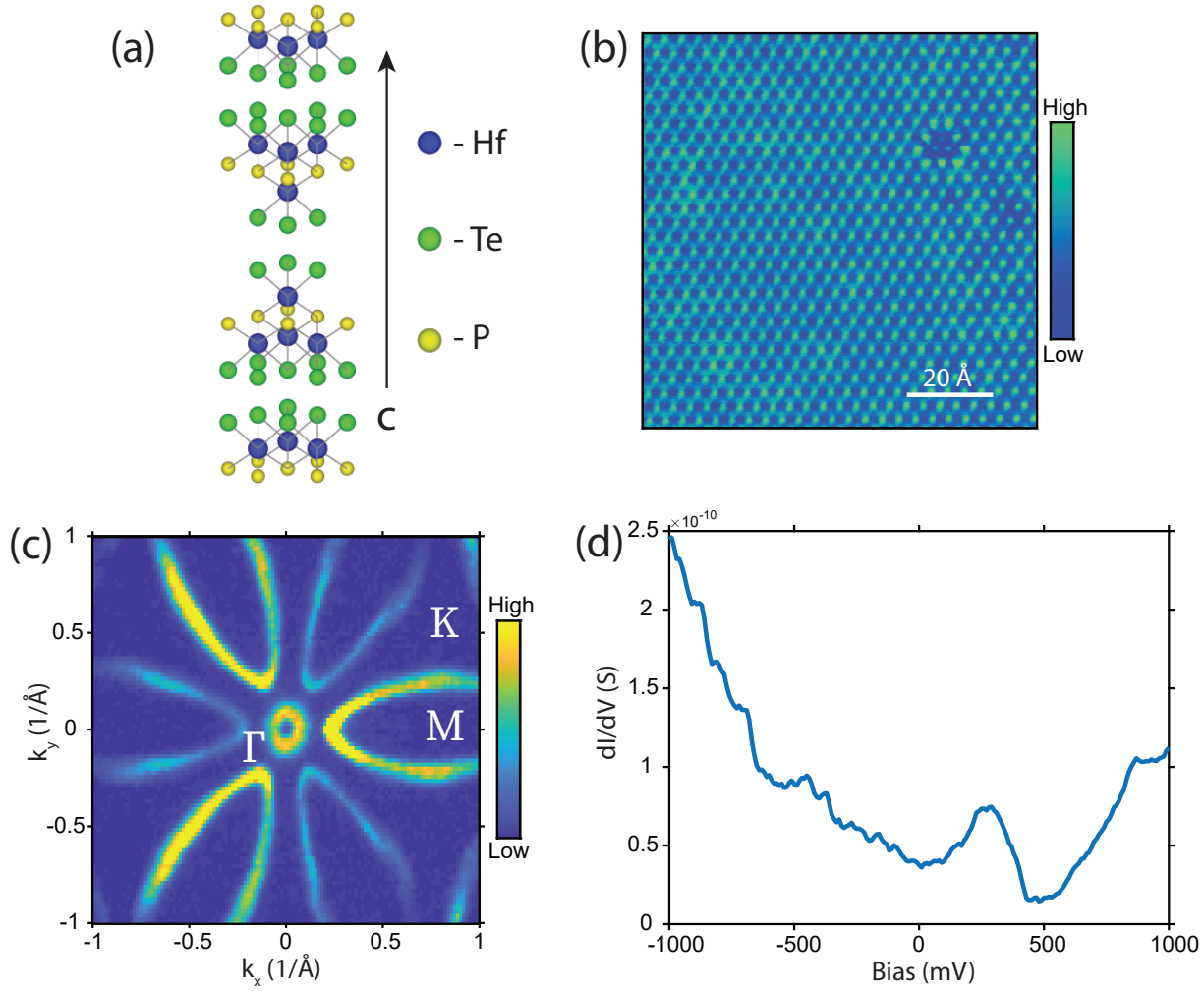

Figure 2.4: Hf_2Te_2P characterization: (**a**) Crystal structure of Hf_2Te_2P. (**b**) STM topography taken at $-120\,\mathrm{mV}$ sample bias and $700\,\mathrm{pA}$ current setpoint. (**c**) Fermi surface of pristine sample measured by ARPES. (**d**) STS measured dI/dV spectrum with current and bias set points of $450\,\mathrm{pA}$ and $-1.5\,\mathrm{V}$.

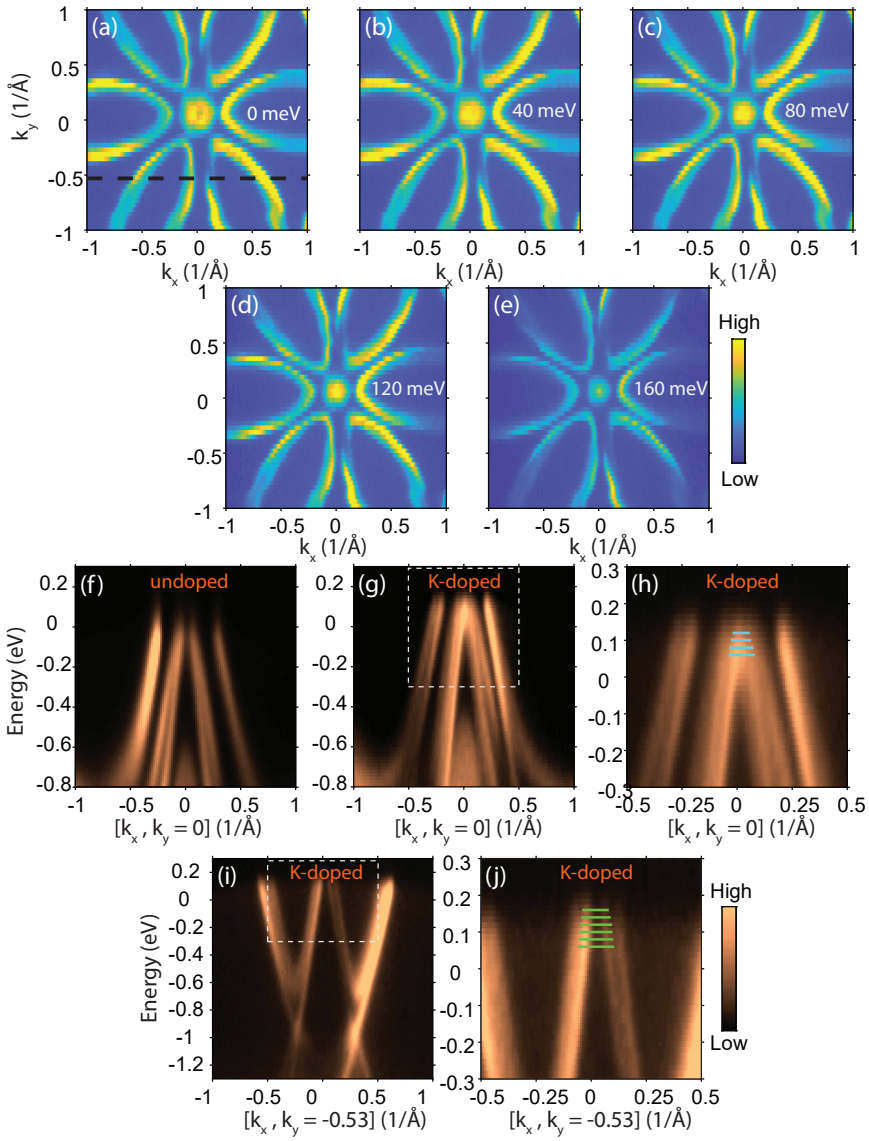

Figure 2.5: K-doped ARPES: (**a**-**e**) ARPES measured constant-energy contours of the K-doped sample for different positive energy values. (**f**) Band structure of the undoped sample along Γ-M. (**g**) Band structure of the doped sample along Γ-M. (**h**) Region highlighted by the gray box in (g) showing the Q-vectors (cyan lines) associated with the hole pocket centered at Γ for four different energies. (**i**) Band structure along the direction of the dotted line in (a). (**j**) Region highlighted by the gray box in (i) showing the Q-vectors (green lines) for five different energies. The appearance of duplicate bands in the K-doped data, when compared to the undoped sample, (f) and Fig. 2.4(c), can be attributed to multiple facets of the cleaved surface.

the local density of states (LDOS) are much larger than the inter-atomic distance and are strongly energy-dependent. This last behavior is typical of quasiparticle interference where the modulations are characterized by an energy dependent wave vector $\boldsymbol{Q}(E) = \boldsymbol{k}_f(E) - \boldsymbol{k}_i(E)$, where $\boldsymbol{k}_{i,f}(E)$ are determined by the band structure. The two-dimensional Q-space structure of the LDOS is obtained by Fourier transformation of the STS maps, $\tilde{g}(Q, E)$, as seen in Figs.2.6(d-f). Note that $\tilde{g}(Q, E = 80\,\text{eV})$ roughly features a hexagonal shape, while $\tilde{g}(Q, E = 160\,\text{eV})$ more closely matches a star shape, Fig. 2.6(d-f), which more clearly conveys the energy dependence of the real-space QPI patterns. While other techniques that can also probe the unoccupied electronic states, such as inverse photoemission, two-photon photoemission spectroscopy and time-resolved ARPES, suffer from limitations in energy resolution, difficulties in the interpretation of non-equilibrium states and related dynamics, and many be restricted to work only for a narrow range of materials. On the other hand, the QPI and K-doped ARPES measurements used in this study probe the sample in its equilibrium state and can be done with high energy resolution and to a wider range of materials.

The results of the ARPES and STS measurements can be compared quantitatively for energies between E_F and 160 meV, which is the range accessed by both K-doped ARPES and STS. Line cuts of $\tilde{g}(Q, E)$ along the two high symmetry directions show distinct peak features on top of a large background. For example, a linecut along $[Q_x = 0, Q_y]$ at 240 meV reveals a distinct peak at 0.09 (1/Å), Fig. 2.7(a-b). From $\tilde{g}(Q, E)$, QPI dispersion maps can be calculated along the two high symmetry directions, Fig. 2.7(c). In the 0 to 220 meV range two peaks that disperse inwards as a function of energy are observed. A detailed comparison to the ARPES data indicates that the inner dispersive peak matches the intra-pocket distance across Γ, while the outer peak dispersion more closely matches the separation between adjacent electron-pockets *petals* – see the cyan and green circles in Fig. 2.7(c),

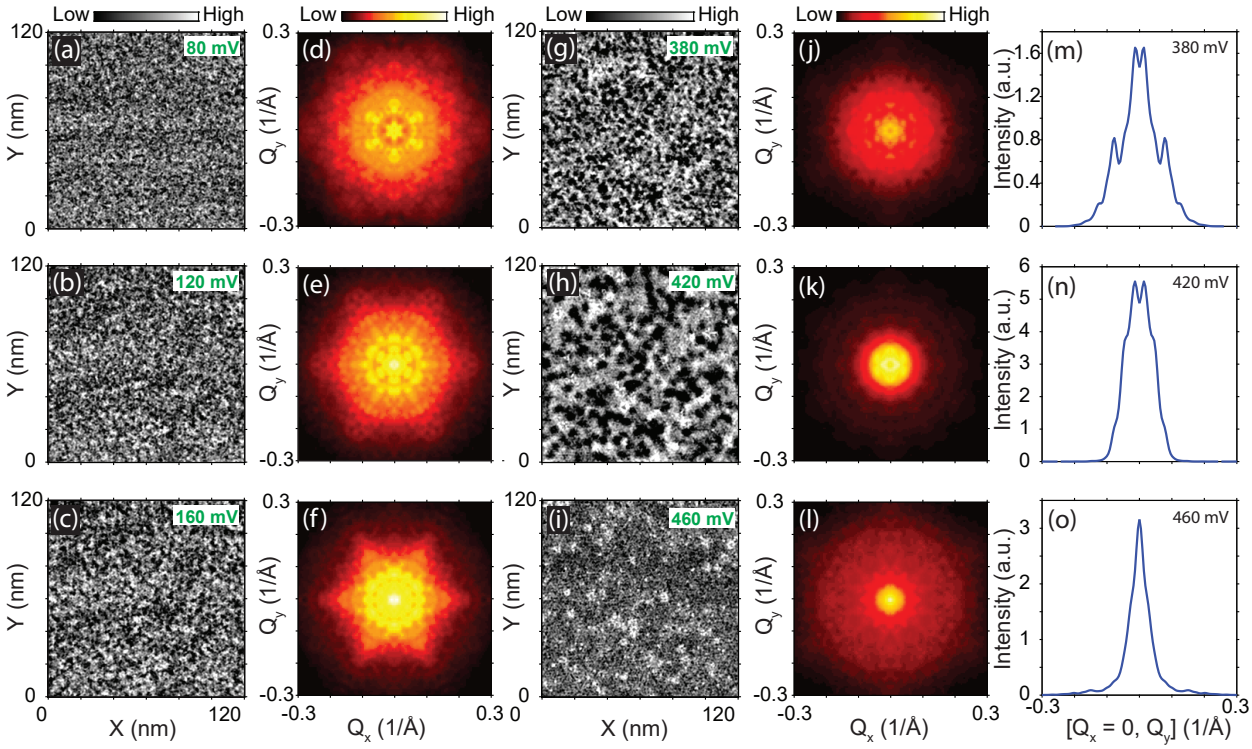

Figure 2.6: dI/dV Maps: (**a-c**) STS maps showing the real-space LDOS near 170 meV. (**d-f**) Fourier transforms of (a-c). (g-i) STS maps near 420 meV. (**j-l**) Fourier transforms of (g-i). (**m-o**) Line cuts along $[Q_x = 0, Q_y]$. The bias and current values were set to 800 mV and 500 pA respectively, and the dI/dV signal was measured via a lock-in technique with a modulation amplitude of 10 mV.

which correspond to the cyan and green lines in Figs. 2.5(h,j). In fact, ARPES cuts along $[k_x, k_y = -0.53]$ (1/Å) indicate a linear dispersion which extrapolate to a node near 220 meV, Figs. 2.5(i,j). A similar state has been observed in Zr_2Te_2P, with spin-orbit coupling expected to open a gap since the crossing is located away from time-reversal invariant momenta and is not protected by any crystalline symmetry [29]. The STS measurements in this study do not resolve the presence of a gap at 220 meV, although the resolution was limited to 10 meV. Contrary to the outer peak, the inner QPI feature originates from the band centered at Γ, a time-reversal invariant point, as further confirmed by the excellent agreement with reported band structure calculations (blue line in Fig. 2.7(c)) [30]. The triple quantitative agreement between STS, ARPES and theory confirms the presence of a Dirac-like dispersion centered at 170 meV.

2.3.2 SS2

SS2 is a strong topological SS predicted near 460 meV. Although ARPES cannot access this state, even with K-deposition, it can be resolved with STS measurements. Although QPI signals can be the result of multiple surface or bulk bands, the calculated band structure of Hf_2Te_2P indicates that the highest energy SS near Γ exists inside a large bulk pseudogap (≈ 0.13 eV), consistent with the observed minimum in the tunneling DOS, Fig. 2.4(e). Focusing on that energy region, the data show a dramatic increase in the characteristic wavelength of the QPI pattern as the bias is varied from 380 meV to 420 meV, see Fig. 2.6(g-h). The same trend is observed in the Fourier transforms, Fig. 2.6(j-k) where a circular pattern shrinks towards $Q = 0$, reflecting the expected QPI pattern from an isolated Dirac cone. Then, the expectation is that precisely at the crossing $\tilde{g}(Q)$ should display a single peak at $Q = 0$, which becomes broad in the presence of disorder. Indeed, the real space STS data in Fig. 2.6(i)

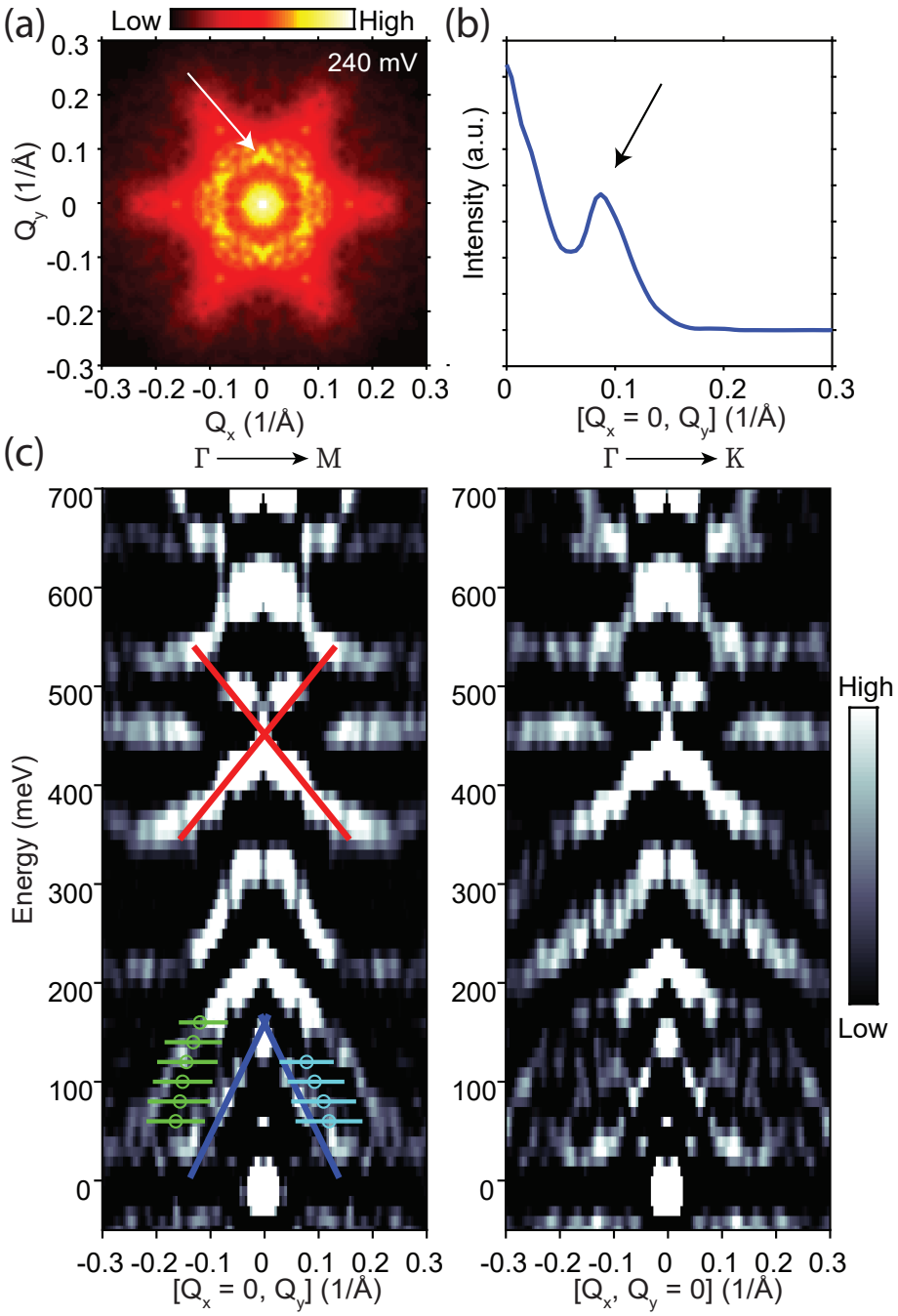

Figure 2.7: QPI band structure: (**a**) Fourier transform of the STS map at 240 mV. (**b**) Line cut of (a) along $[Q_x = 0, Q_y]$, showing a distinct peak at $Q_y = 0.09\,(1/\text{Å})$. (**c**) QPI dispersion maps along the Γ-M and Γ-K directions. The ARPES measured Q-vectors are overlaid by cyan and green dots (with solid line error bars) for the dispersion curves displayed in Fig. **??**(h) and (j) respectively. Q-vector dispersions from the band-structure calculations along Γ-M are represented by the red and blue lines.

shows a spatially inhomogeneous LDOS, due to the structural defects of the crystal, and a single central peak in the Fourier transform data, Fig. 2.6(l). This trend is summarized in Figs. 2.6(m-o), which display line cuts of the data in Figs. 2.6(j-l), showing $Q_y \neq 0$ peaks converging to a single point at 460 meV. In the absence of a predominant $Q \neq 0$ QPI signal at 460 meV, $\tilde{g}(Q)$ displays a weak halo, Fig. 2.6(l,o), that stems from the intrinsic inhomogeneity of Hf_2Te_2P. Indeed, identical spatial patterns were observed in both the $\tilde{g}(Q, E = 460\,\text{meV})$ and the topographic map over the same area, which confirms the non-QPI origin of the halo in Fig. 2.6(l). Thus the intensity observed in the second-derivative map in Fig. 2.7(c) at $E = 460$ meV and $Q \approx \pm 0.17\,(1/\text{Å})$ is not indicative of an additional band. Importantly, there is very good agreement between the energy-dependent QPI signal and band structure calculations (red lines in Fig. 2.7(c)) in this region, revealing the presence of the surface state with a node at 460 meV above E_F.

2.4 Discussion

The combined STS and ARPES measurements and their remarkable agreement with previous band structure calculations indicate the presence of TSSs above the Fermi level in Hf_2Te_2P. Although the topological nature of the various SSs and their spin-texture still requires more direct evidence from, for example, spin-polarized ARPES [43] or STS near extended defects [44], the remarkable agreement to the reported band structure calculations strongly suggests their topological nature. If these states are to be harnessed towards novel technologies they need to be tuned to E_F by either chemical doping or surface gating. Here, the states above E_F uncovered by this study may provide a more direct path to these technologies than the previously measured states at -0.9 eV. Also, the surface state centered at 460 meV is observed in the absence of other bands in the QPI measurement, suggesting

a small contribution from the bulk, although only detailed measurements of the electronic bulk properties would confirm this. Still, a high surface to bulk conductance ratio could be achieved in Hf_2Te_2P, since the strong topological nature of the surface state at 460 meV originates from the band inversion of Hf-d and Te-p orbitals, in contrast to traditional topological insulators. Note that the mixing Hf-d and Te-p orbital character, and its topology, may be tuned by chemical substitution, with the substitution of Hf (e.g. by Zr or Ti) controlling the d-orbitals and the substitution of Te (e.g. by Se) regulating the p-character – not to mention the modification of lattice parameters by doping the P site (e.g. by As) or by chemical intercalations between layers. Finally, since the current topological insulators suffer from contaminant conducting bulk channels that bypass the topologically protected surface states, the topological states uncovered by this study may offer an alternative avenue for future applications.

Chapter 3

Resonant x-ray scattering study of charge order in $La_{1.475}Nd_{0.4}Sr_{0.125}CuO_4$ under uniaxial stress

This project began in 2017 as an effort to measure the effect of stress on the charge order in $Bi_2Sr_2CaCu_2O_{8+x}$ using a piezoelectric strain device. Following this endeavour, Santiago Blanco-Canosa suggested that we try applying stress to $La_{1.475}Nd_{0.4}Sr_{0.125}CuO_4$ to measure the effects on the charge stripes and low-temperature tetragonal phases. The project was done in collaboration with Alex Frano's research group using the Canadian Light Source and BESSY-II synchrotron facilities. The results were published in 2021 as a letter in Physical Review Research [18].

3.1 Introduction

Cuprate high-temperature superconductors may be the quintessential example of a strongly correlated quantum system, featuring a complex interplay between broken symmetry states, often referred to as intertwined orders [45, 46]. This rich interplay is evident in the charge order (CO) state: a periodic modulation of charge that is intertwined with superconductivity, magnetism, the crystal structure, and nematicity (four-fold C_4 to two-fold C_2 symmetry breaking [47]). These various links between ordered states and CO are perhaps most clearly observed in the '214' family of La-based cuprates. *(i)* CO and magnetism emerge intertwined in the form of stripes. *(ii)* The stripes are C_2 symmetric, with their orientation alternating by 90° between adjacent CuO_2 planes [48]. *(iii)* The stripes are strongly pinned to the low temperature tetragonal (LTT) crystal structure, which stabilizes the alternating pattern [49, 50]. *(iv)* Finally, the stabilization of stripes occurs in concert with the suppression of three-dimensional (3D) superconductivity, which results from a frustration of the Josephson coupling between adjacent CuO_2 layers [51, 52]. Determining how all these ordered states are interconnected is a major challenge in the field of high-temperature superconductivity.

There are different methods to tune the intertwined orders in the cuprates. Typically, a magnetic field [14, 53], chemical doping or isotope substitution [54, 55], or pressure [56] are used to adjust the relative strengths of the ordered states. For instance, the application of 1.85 GPa of hydrostatic pressure to $La_{1.875}Ba_{0.125}CuO_4$ decouples the LTT and CO phases, suppressing the former while allowing the latter to survive with an onset temperature of 35 K [57]. However, controlling the rotational symmetry of the correlations in the CuO_2 planes requires a tuning parameter that couples directionally to the electronic degrees of freedom. This can be achieved with the uniaxial application of pressure, or stress, which has recently become the focus of several cuprate studies. For example, recent experiments on

$YBa_2Cu_3O_{6+y}$ indicate that attaining uniaxial strain around 1% can modify the inter-layer interaction of the CO and its coupling to acoustic phonons [58, 59]. In the '214' family, uniaxial stress has repeatedly been shown to increase the onset temperature of superconductivity [60–63]. A small value of uniaxial stress, approximately 0.05 GPa, dramatically increases the onset of 3D superconductivity in $La_{1.885}Ba_{0.115}CuO_4$ (LBCO-115) from 6 K to 32 K [63]. Remarkably, the same application of uniaxial stress also reduces the onset of spin stripe order from 38 K to 30 K. These opposing effects between superconductivity and spin stripes highlight the importance of uniaxial stress experiments to the study of intertwined orders. Still, diffraction experiments that directly measure the effects of uniaxial stress on charge stripe order and the LTT structure in the La-based cuprates have not been reported.

This study reports Cu L_3- and O K-edge resonant x-ray scattering (RXS) measurements of CO and the LTT structure in $La_{1.475}Nd_{0.4}Sr_{0.125}CuO_4$ (LNSCO-125) under the influence of modest uniaxial stress, approximately 0.1 GPa, applied along the a axis of the LTT structure (*i.e.* along the Cu-O bond direction). First, a detailed zero-stress control experiment on LNSCO-125 is reported, where a precursor charge-order (PCO) peak is observed above the onset of stripes near 75 K and detectable up to at least 150 K. Upon introducing uniaxial tensile-stress, the onset of the LTT phase (T_{LTT}) is reduced by 29 K, from 63 K to 34 K. Additionally, the onset of stripe order decreases by approximately 50 K, from $\approx$ 75 K (T_{LTT} + 12 K) in the absence of strain to $\approx$ 23 K (T_{LTT} − 9 K) in the presence of strain. This overall shift is larger than the one observed for T_{LTT}, which likely reflects the competition between CO and superconductivity. An additional offset of approximately 6 K is observed between the onset of charge stripes along the a and b directions. Despite the effects of stress on the LTT and the charge stripe phases, there is no appreciable modification of the PCO. Altogether, the experiments not only show that a small amount of uniaxial stress triggers responses from

the various intertwined orders, they also establish uniaxial stress as a powerful tool to control the electronic properties of LNSCO-125.

3.2 Methods

3.2.1 Crystal structure

The synthesis was performed by Wei Peng and Alexander Komarek. Single crystals were synthesized by floating zone and previously characterized by means of resonant x-ray scattering and magnetometry [64]. LNSCO-125 hosts several classic features of La-based cuprates near 1/8 hole doping including the 1/8-anomaly, whereby the superconductivity is suppressed as static spin and charge orders develop [65, 66]. Despite this, the samples remain superconducting with a transition temperature of $T_c = 5\,\mathrm{K}$ [64]. Additionally, they undergo a structural orthorhombic-to-tetragonal phase transition. Above $\approx 65\,\mathrm{K}$, in the absence of uniaxial stress, the samples are in the low temperature orthorhombic (LTO) phase, where the CuO_6 octahedra tilt about an axis parallel to the [110] direction, which is 45° from the Cu-O bond direction. At lower temperatures, in the LTT phase, the CuO_6 octahedra tilt about axes parallel the Cu-O bond directions [67, 68]. Importantly, in the LTT phase the tilt axis alternates between [100] and [010] through consecutive CuO_2 planes, Fig. 3.2. Thus, while the LTT is a globally tetragonal phase, it is actually two-fold C_2 symmetric within each CuO_2 plane, which provides a natural motif to stabilize the stripe order.

3.2.2 Strain device

The strain device was developed with the help of Junhui Shi and Eduardo da Silva Neto and is based on the design of Hicks et al. [69]. It consists of three piezoelectric stack actuators

(APC International, Ltd. Pst150) and machined Grade 2 titanium parts. The parts were assembled using EPO-TEK® H74F epoxy. One end of each of the three piezo stacks is fixed to a rectangular base, as shown in the schematic in Figure 3.1(a). A fixed sample holder is attached to the other end of the middle stack and the outer stacks are attached to a U-shaped frame containing an adjustable sample holder to accommodate samples of different lengths. The gap of the strain device is set to be slightly larger than the length of the sample. Epoxy (EPO-TEK® H74F) is then applied to the edges of the gap and the sample is situated on the epoxy such that it does not make contact with the titanium. The coefficient of thermal expansion of the epoxy is an order of magnitude larger than those of the sample and titanium, so while the contraction of the sample gap (i.e. titanium) and crystal are similar, the larger contraction of the epoxy causes the sample to be stretched relative to an unconstrained sample. While the strain device is designed to produce stress through the application of voltage to the piezo stacks, the large effects reported in the main text were observed in the absence of applied voltage. Only a few attempts were made to observe the effects of applying voltage to the piezo devices, however, a change in the lattice constants was not observed upon applying voltage at low temperature. This is likely due to several factors including the reduction of the piezoelectric effect at low temperatures and the large cross-sectional area (750 μm x 150 μm) of the LNSCO-125 sample. Indeed, samples with needle-like geometries (i.e. smaller cross-sectional area) are likely needed, as in other uniaxial strain experiments [58, 59]. Given the limited amount of beam time for the experiments, the time was focused on the characterization of the various effects on stripes and LTT-LTO transition, which were due to differential thermal contraction alone.

The strain due to thermal contraction, ϵ_{xx}, along the a axis (parallel to the Cu-O bond direction) of the lattice can be determined by measuring the change in the lattice constants of the samples from the position of an in-plane Bragg peak (BP). The (103) BP was measured

at high and low temperature by performing θ-2θ scans with a photon energy of 2200 eV, Fig. 3.1(b). Sets of measurements were taken at the beginning and end of the beam time shifts corresponding to cooling and warming the samples. Upon cooling, a difference of $\Delta 2\theta = 0.145$ degrees was observed in the center-of-mass position of the peaks of the stress and control samples at low temperature, while the difference upon warming was $\Delta 2\theta = 0.045$ degrees. This yields average difference of 0.095 ± 0.05 degrees in 2θ, which corresponds to a difference in the change of the in-plane lattice constant of 0.046 ± 0.026 %. Additionally, the (002) BP was measured at high and low temperatures to determine the change in the out-of-plane lattice constant, c, due to thermal contraction and Poisson's effect. This data was incorporated into the calculation of the in-plane lattice constant to account for their influence on the position of the (103) peak (see Appendix B and Equation B.11 for additional details on determining lattice constants from BPs).

To simulate the stress produced by the strain device a COMSOL Multiphysics® model was constructed by Zeke Zhao, as shown in Figure 3.1(c). This simulation incorporates both the elastic moduli and coefficients of thermal expansion of the titanium, epoxy, and LNSCO-125 crystal, as well as the arrangement of the sample and epoxy within the gap. A net tensile-strain pattern is observed across the top surface of the sample at 70 K with an average value of 0.0294 %, which is of the same order of magnitude as measured by the BPs.

The following parameters were used for Young's modulus (Y) and the coefficient of thermal expansion (α) of the different materials in the simulation: H74F Epoxy - $Y = 2.4 \cdot 10^{10}$ Pa and $\alpha = 2 \cdot 10^{-5}$ (EPO-TEK® H74F Product Information Sheet), LNSCO-125 - $Y = 2.5 \cdot 10^{11}$ Pa [70] and $\alpha = 5.02 \cdot 10^{-6}$ (from the control sample BPs), titanium - $Y = 1.161 \cdot 10^{11}$ Pa and $\alpha = 6.51 \cdot 10^{-6}$ (from the COMSOL Material Library). The value of α for LNSCO-125 obtained from the Bragg peaks is consistent with values reported for $La_{2-x}Sr_xCuO_4$ [71]. Young's modulus of the epoxy was increased by a factor of 6 (from

$4 \cdot 10^9$ Pa to $2.4 \cdot 10^{10}$ Pa) at 70 K to be consistent with the temperature dependence reported for other epoxies [72].

3.2.3 RXS

The resonant x-ray scattering experiments were performed by Morgan Walker, Alejandro Ruiz, Santiago Blanco-Canosa, Alex Frano, Eduardo da Silva Neto, and myself at two different beamlines: UE-46-PGM1 at BESSY II with the assistance of Enrico Schriele and 10ID-2 (REIXS) at the Canadian Light Source with the assitance of Ronny Sutarto and Feizhou He; additional experiments were carried out at beamline UE-56/2-PGM2 of BESSY II with the assitance of Christian Schüßler-Langeheine using the Resonant Scattering Station and beamline 12.3.2 (microdiffraction) at the Advanced Light Source with the assistance of Nobumichi Tamura. The charge order (CO) scans were collected as rocking curves with the detector at a fixed angle of $2\theta \approx 148$ degrees, corresponding to $L \approx 1.7$ (r.l.u.) at the peak position. The profile of the background of each rocking curve is subject to several systematic effects, including the angular dependence of the fluorescence background emission and the projection of the incoming photon beam onto the sample surface. To mitigate this systematic error, scans at each temperature were averaged 3 to 10 times, with measurements of the precursor charge-order requiring greater statistics; these sets of measurements typically took 2 hours each. The averaged scans were adjusted via vertical translation and linear slope subtraction to best match the background profile of a fourth-degree polynomial fit of a high-temperature background curve. The high-temperature background fit was then subtracted from each curve, and the resulting peaks were fit to a Lorentzian function. The peak intensities shown in Figure 3.5(a) are the peak values of the Lorentzian fits.

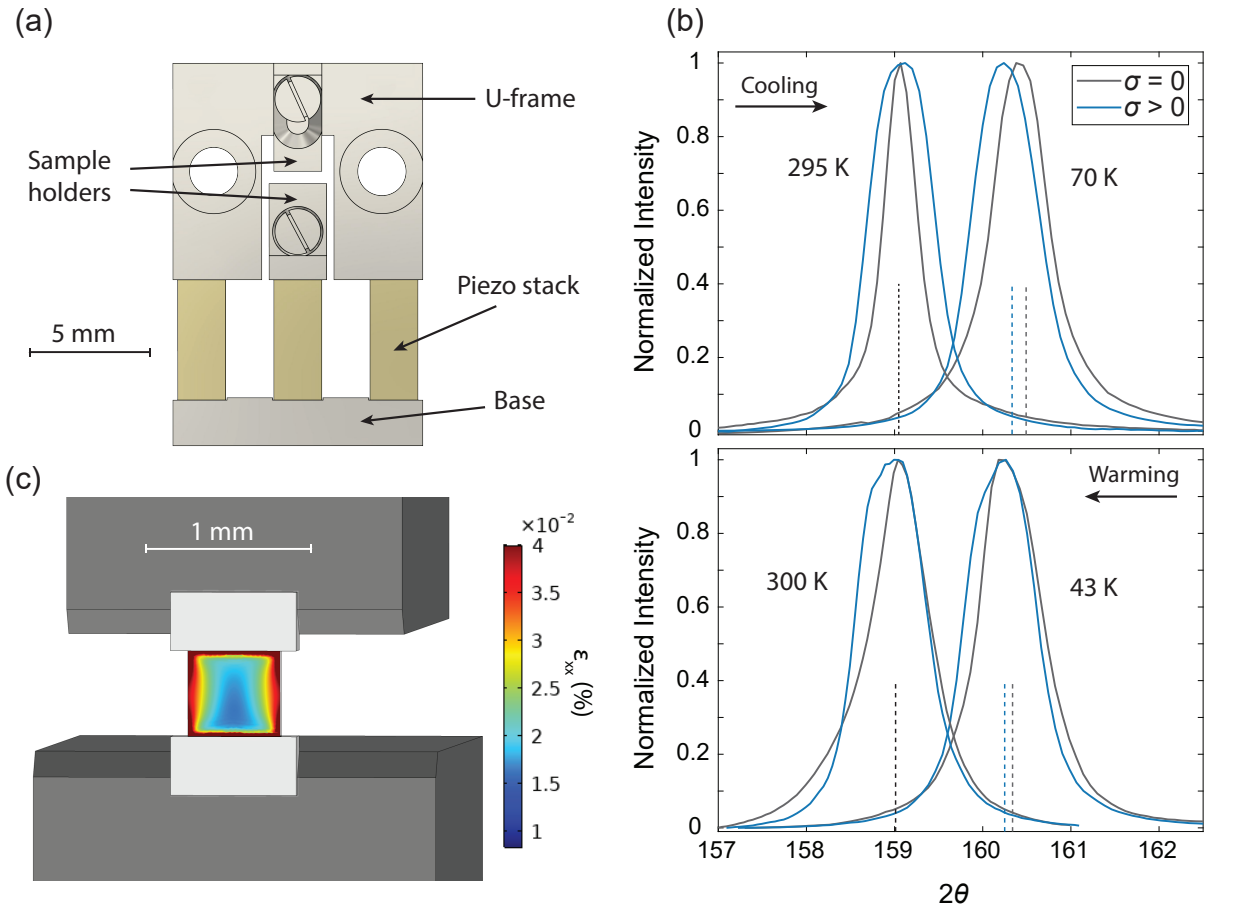

Figure 3.1: Strain measurements: (**a**) A schematic diagram of the strain device. (**b**) (103) Bragg peaks of the control and stress samples at high and low temperatures. The smaller change in 2θ of the stress sample is a consequence of tensile strain. Measurements shown in the top panel were performed upon cooling and the bottom panel upon warming. The dotted lines indicate the center-of-mass positions of the peaks; black corresponds to the high temperature positions and blue and gray correspond to the low temperature positions of the stress and control samples respectively. (**c**) A COMSOL Multiphysics® model of the ϵ_{xx} strain component at 70 K showing a tensile strain pattern on the surface of the sample. The titanium sample holders are dark gray and the epoxy is light gray.

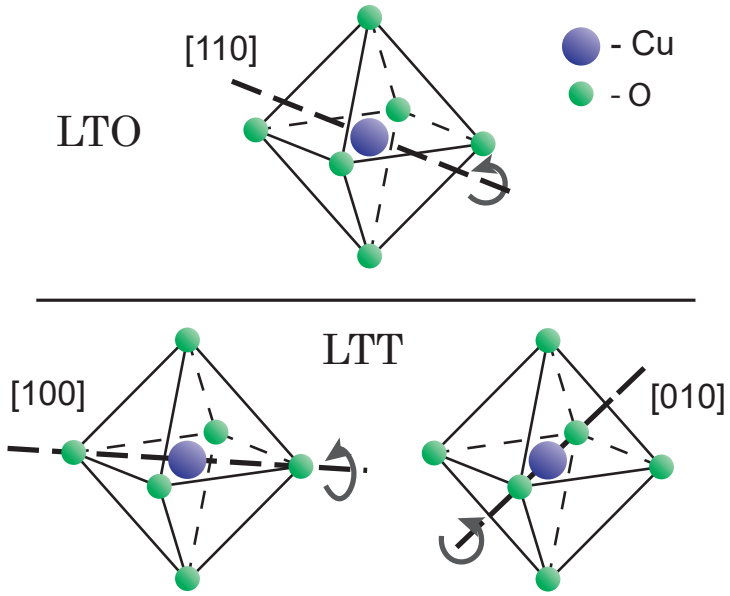

Figure 3.2: LTT and LTO phases: A diagram depicting the CuO_6 octahedral tilts in both the LTO and LTT phases. In the LTO phase, neighboring octahedra tilt in opposite directions (clockwise and counter-clockwise) along the [110] direction. In the LTT phase, adjacent CuO_2 layers have orthogonal tilts along the [100] and [010] directions.

3.3 Results

Previous RXS experiments on LNSCO-125 indicate the appearance of stripe order at approximately T_{LTT} [73]. Figure 3.3(a) shows the temperature evolution of the CO peak at $q_{||} = q_{\mathrm{CO}} = 0.23\,\mathrm{rlu}$ (reciprocal lattice units) in LNSCO-125, showing a clear and rapid enhancement below 75 K, corresponding to charge-stripes. Interestingly, these RXS experiments also reveal a PCO peak at q_{CO} for temperatures above 75 K, albeit with much lower intensity when compared to the low-temperature signal. While it is difficult to determine the onset temperature for the PCO, a clear evolution of the peak can be observed up to 200 K, Fig. 3.3(b), which is better visualized by subtracting the 300 K curve, Fig. 3.3(c).

It is important to note that since the RXS experiments are done in energy-integrated mode, the PCO may originate from both elastic (static) and inelastic (dynamic) correlations. In fact, high-temperature dynamic CO signals have recently been observed in many cuprates, including other La-based systems [74, 75]. While it may be tempting to assign the same rotational symmetry of the charge stripes to the PCO, such correspondence has not been experimentally verified. Therefore, the two signals are distinguished as described in the previous paragraph, and the general phenomenon is referred to simply as CO. As discussed later, there are no modifications to the PCO due to uniaxial stress in the experiments despite observing significant effects to the LTT phase and charge stripes.

To investigate what happens to the CO and the LTT phase when the LNSCO-125 sample is perturbed with extrinsic uniaxial stress, $\sigma \neq 0$, the crystal is embedded in an apparatus whose geometry explicitly breaks C_4 symmetry, Fig. 3.4(a). The sample is constrained on two-edges across a gap using expoy in a device constructed of machined high-purity titanium. Differential thermal contraction occurs upon cooling due to the different coefficients of the thermal expansion of the sample, epoxy and titanium, which causes the LNSCO-125 crystal to be uniaxially stretched relative to an unconstrained crystal. The experimental setup also includes a second sample mounted directly on one of the faces of the device using silver paint, which allows for control measurements on a $\sigma = 0$ sample in the same experiment, Fig. 3.4(a). (Note that σ refers to externally applied stress and does not include the intrinsic stress due to the thermal contraction of the crystals themselves.) Unlike many strain experiments that cannot directly probe the lattice parameters, the lattice constants can be accessed by measuring the Bragg peaks of the LNSCO-125 crystal. The Bragg peak measurements yielded strain values of $\approx 0.046 \pm 0.026\,\%$. Using $C_{11} = 232\,\mathrm{GPa}$ for the elastic modulus [76], the stress can be calculated as approximately $\sigma = 0.11 \pm 0.06\,\mathrm{GPa}$. Additionally, a multiphysics simulation was constructed that incorporates all key elements of the assembly,

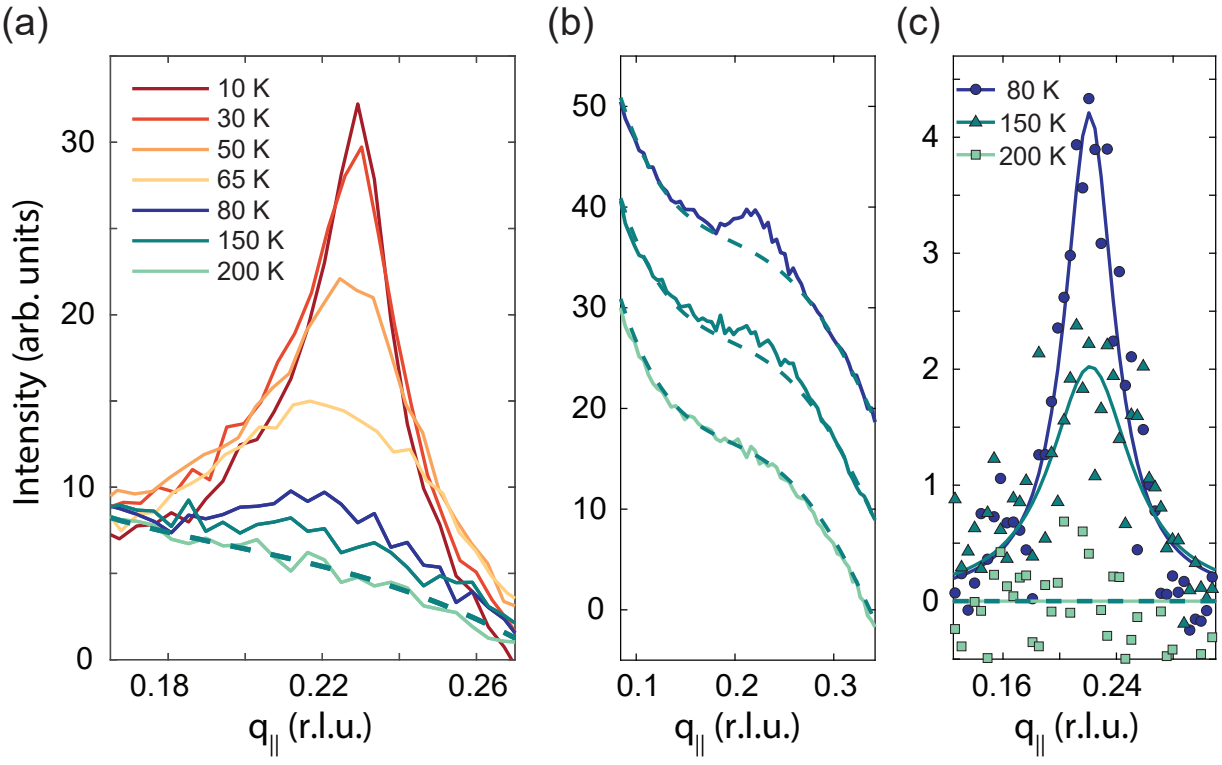

Figure 3.3: Temperature dependence of charge stripes: (**a**) Temperature dependent RXS scans of the CO peak in LNSCO-125. The gray dashed line is a polynomial fit of the high-temperature background curve measured at 300 K. (**b**) RXS scans in the LTO phase, which show a gradual temperature dependence. (**c**) Lorentzian fits of the background-subtracted curves shown in (b).

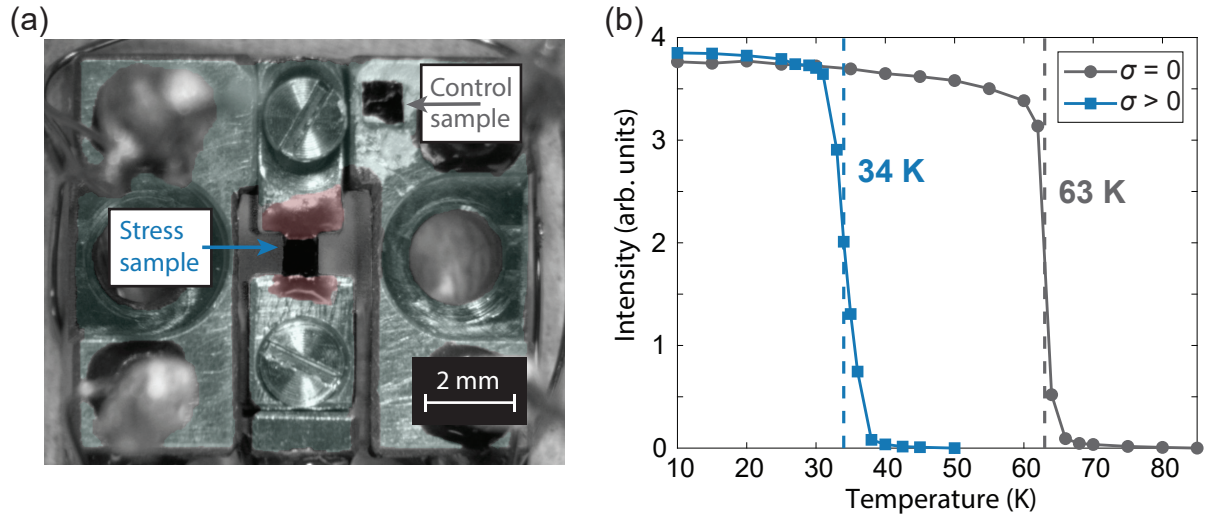

Figure 3.4: Effect of Strain on T_{LTT}: (**a**) An image of the titanium strain device and LNSCO-125 crystals. The stress sample is mounted in the center across a gap using a stiff epoxy and the control sample is mounted on the titanium using silver paint. (**b**) Temperature dependence of the (001) Bragg peak on the apical O K-edge in both the stress and control samples corresponding to the LTT phase transition. The transition temperature is suppressed by 29 K with the applied stress.

including the thermal and elastic properties of the materials, as well as the geometry of the assembly [77]. The simulation produces an approximately uniform tensile strain pattern of the same order of magnitude as measured by the Bragg peaks when the apparatus is cooled to 70 K. Although the amount of stress is relatively small, it is comparable in magnitude to the compressive stress used in the LBCO-115 experiments mentioned above, which were shown to have significant effects on the superconductivity and spin-stripe order [63].

A striking consequence of $\sigma \neq 0$ in the experiments on LNSCO-125 is the dramatic reduction of T_{LTT} from 63 K to 34 K, Fig. 3.4(b). This is directly seen in the experiments via apical O K-edge RXS measurements of the (001) Bragg peak (in Miller index notation), whose resonant cross-section is an increasing function of the octahedral tilts in the LTT phase [73]. The reduction of T_{LTT} can be understood as a consequence of uniaxial stress, which spoils the global tetragonality of the LTT phase. Although it still emerges at low temperatures,

the experiments unveil a remarkable response of the LTT structure in LNSCO-125 to the application of uniaxial stress.

In principle, uniaxial stress could result in the transition of the macroscopic crystal into a mixed LTO/LTT phase or a decrease in the LTT octahedral tilt angle, as hypothesized from measurements of the magnetic properties of LBCO-115 [63]; neither effect is resolved in these measurements. First note that the intensity of the (001) Bragg peak, whose cross-section is an increasing function of the octahedral tilt angle, appears unchanged by σ at 10 K. This indicates that, within the LTT phase, the structure is unaffected by stress. Second, the LTO-LTT transition remains sharp with non-zero σ, which suggests that the stress sample enters the LTT phase in a rather uniform fashion. While the uniformity of the strain field on the sample may vary between different uniaxial strain setups, these experiments do not provide evidence of a mixed phase or reduced octahedral tilt angle.

Within the same experiment, the temperature dependence of the CO in the stressed LNSCO-125 crystal can also be tracked, which is summarized in Fig. 3.5(a). A consequence of uniaxial stress is the reduction of the onset temperature of charge stripes by 50 K, which is larger than the change of 29 K observed for T_{LTT}. If the only effect of uniaxial stress was the suppression of T_{LTT}, one might have expected the onset of charge stripes to have changed by the same value (i.e. 29 K). However, the additional shift of 21 K suggests that one should also consider interactions with additional intertwined orders, such as superconductivity. Although measurements of the superconducting T_{c} were not performed in this experiment, previous studies have measured the response of superconductivity to uniaxial stress in similar materials. Uniaxial stress on the order of 0.05 GPa has been shown to increase T_{c} by 8 K in LNSCO-120 and by 10 K in LBCO-115 [60, 63], showing that superconductivity is enhanced in tandem with the suppression of the LTT phase. Additionally, cuprates that lack a similar structural transition, such as $Bi_2Sr_2CaCu_2O_{8+x}$ and $YBa_2Cu_3O_{6+y}$, exhibit com-

petition between superconductivity and CO [13–15]. Together, the suppression of the LTT phase and the enhancement of superconductivity would account for the larger suppression of the onset of stripes relative to the suppression of T_{LTT}.

In addition to the effects on stripe order due to its intertwining with the LTT phase and superconductivity, uniaxial stress may also directly influence the pinning of stripes along a and b. For example, given the C_2 symmetry of stripe order, one may expect that a finite σ in the absence of an LTT phase would cause the onset temperatures of stripes along a and b to split. Indeed, this split is resolved by the temperature dependent RXS measurements, Fig. 3.5(a). This is seen more clearly by directly comparing the RXS data along the two directions, Figure 3.5(b), which shows that at 23 K the peak along a (parallel to the applied stress) has already entered the charge stripe phase, while the peak along b is still very similar to the peak in the high-temperature phase – compare to the 35 K data. Eventually, at 15 K the two signals approach the same saturation value, which may indicate that the LTT structure has suppressed the effects of $\sigma \approx 0.1$ GPa at this temperature. Nevertheless, the measurements show that uniaxial stress can be used to pin the direction of stripes in the CuO_2 plane.

While these measurements show a delicate balance between charge stripes, superconductivity and structural distortions, a direct effect of uniaxial stress on the PCO is not clearly resolved. Just above the onset of charge stripe order, the intensities of the RXS peaks at q_{CO} are indistinguishable between the stress and control samples. Additionally, a clear difference in the PCO along a and b in the stress sample is not observed – for example see the 35 K data in Fig. 3.5(b). Figure 3.5(a) suggests that the onset of the PCO at high-temperatures may be impacted by the application of stress along a. However, there are several complications that prevent one from drawing such a conclusion. First, as mentioned above, the PCO evolves very slowly with temperature, which makes the assignment of an onset temperature

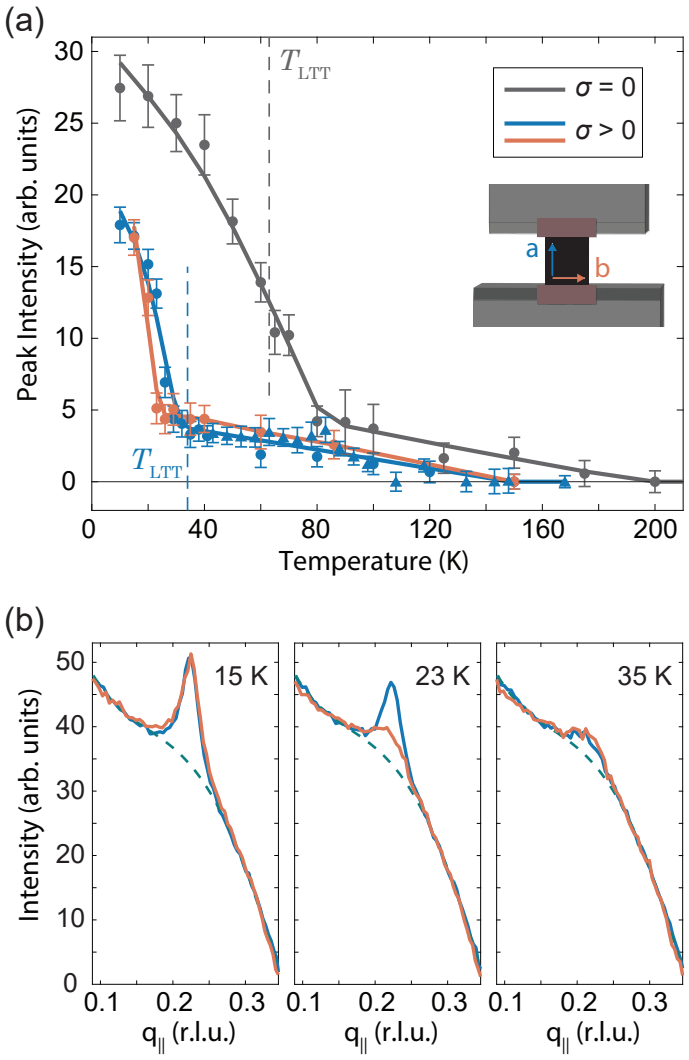

Figure 3.5: Effect of strain on charge stripes: (**a**) Temperature dependence of the CO peaks in the stress and control samples. The solid lines serve as guides to the eye. The dashed lines correspond to the LTT transition temperatures determined from Fig. 3.4(b). The inset shows a diagram of the stress sample, where a (blue) and b (orange) indicate the directions parallel to and perpendicular to the direction of applied stress respectively. Measurements of the stress sample along the a direction were performed at two different synchrotrons: measurements from the Canadian Light Source are triangles and measurements from BESSY-II are circles. (**b**) Comparison of RXS scans of the stress sample along the a and b directions near the LTT transition. The gray dashed line is a polynomial fit of the high-temperature background curve measured at 150 K. The onset of the charge stripes along the direction of applied stress precedes that of the perpendicular direction by approximately 6 K.

difficult. Second, the stress produced by the strain apparatus is temperature dependent and there is an estimated 3 to 5 fold decrease in the applied stress from 34 K to 200 K. Third, the comparison of small RXS peaks between the stress and control samples can be influenced by variations in the fluorescence background, which is sensitive to sample surface conditions. The effects of uniaxial stress to the PCO will likely require experiments that tune the stress at a fixed temperature. Altogether, there is no observation of any direct coupling between uniaxial stress and the PCO.

3.4 Discussion

These experiments demonstrate the complex relationship between uniaxial stress, charge stripes and the low-temperature tetragonal structure in LNSCO-125. Increasing σ from zero to 0.1 GPa causes a simultaneous reduction in the onset temperatures of both the LTT phase and charge stripes, as well as a temperature splitting in the formation of charge stripes along the a and b directions. Additionally, the effects of superconductivity need to be included to describe the observations, with the competition between superconductivity and charge order together with the enhancement of T_c under uniaxial stress serving as a natural explanation for the additional suppression of the onset of stripe order with respect to T_{LTT}. Furthermore, larger stress may be necessary to cause significant changes to the PCO. Nevertheless, the relatively small amount of stress necessary to tune the electronic properties of the La-based cuprates near 1/8 hole-doping is quite remarkable. For example, strain on the order of 1.0 % is necessary to modify the properties of charge order in $YBa_2Cu_3O_{6+y}$ [59] or to shift the superconducting transition by 2 K in Sr_2RuO_4 [78, 79]. While achieving 1.0 % strain may be quite challenging and difficult to reproduce, 0.05 % or even smaller is clearly sufficient to

alter the electronic properties of LNSCO-125, which opens new opportunities for switchable devices and precision detectors at the current frontier of technology.

Chapter 4

Nematicity and Electronic Ordering in $FeSe_{1-x}S_x$

This project began in 2019 with the aim of measuring the relationship between nematicity and superconducitivy in $FeSe_{1-x}S_x$. However, upon measuring $FeSe_{0.77}S_{0.23}$ with STS, Morgan Walker, Zeke Zhao, Eduardo da Silva Neto and I observed a static charge pattern near the Fermi level, features that indicate charge ordering. This led to an in-depth characterization of the CO by combining our STS measurements with ARPES performed and the Canadian Light Source and theoretical calculations done by Ilya Eremin's group. The project was completed in 2021 and is currently in the peer review process.

4.1 Introduction

The phase diagram of unconventional superconductors is characterized by the presence of different electronic orders in addition to superconductivity [10, 80]. Among these, the cuprate and iron-based superconductors (IBSCs) are two families of materials that feature similar

types of ordered states [81–83]. In both cases magnetic ground states with antiferromagnetic correlations exist, which for Fe-based systems appear in the form of spin density waves (SDWs). The two systems also feature electronic nematicity, which breaks four-fold C_4 symmetry into a two-fold C_2 symmetric state. Recently, in the cuprates, periodic modulations of the electronic density of states known as charge order (CO) were shown to be ubiquitous across different cuprate families and to also have clear connections to superconductivity [84, 85]. Additionally, CO is often observed as alternating unidirectional short-range domains, pointing to an intrinsic connection to nematicity [86]. Several theoretical and experimental studies indicate that the CO in the cuprates appears as a consequence of strong electron correlations [84, 87–92]. However, the degree to which strong correlations play a role in determining the electronic properties of IBSCs is much less clear and the presence of CO similar to that in the cuprates has not been established in the Fe compounds.

Recently, it has been proposed that one way in which strong electron correlations could appear in IBSCs is through orbital selectivity [93, 94]. In this scenario, some of the five d orbitals that participate in the low energy properties of IBSCs may develop strong correlations while the remaining orbitals stay in the weak coupling limit. Scanning tunneling microscopy and spectroscopy (STM/S) experiments indicate this exact scenario is actually realized in the nematic state of FeSe [95, 96]. Therefore, CO stemming from strong correlations may be possible by tuning the electronic states in this family of IBSCs, for example via S substitution. In $FeSe_{1-x}S_x$, where SDW order is absent, a putative nematic quantum critical point (QCP) is achieved by the substitution of Se for S, which suppresses the tetragonal-to-orthorhombic transition temperature (T_S) to zero at $x = x_c \approx 0.17$ (Fig. 4.2(a))[97–99]. While in other families of IBSCs the superconducting transition T_c is maximum near the nematic QCP, T_c in $FeSe_{1-x}S_x$ reaches a maximum at $x \approx 0.11$ and shows a slight suppression for $x > x_c$,

which is reminiscent of the suppression of T_c in some cuprates caused by the presence of the competing CO.

This study uses STS to directly image the electronic density of states in $FeSe_{1-x}S_x$, revealing CO. These measurements clearly reveal the presence of spatial modulations with an approximate period of 52 Å (0.12 $Å^{-1}$ wave vector) in $FeSe_{0.77}S_{0.23}$ that bear remarkable qualitative similarities to the CO observed in the Bi-based cuprates. Additionally, the STS results are compared to both ARPES measurements and theoretical modeling in order to determine the origin of the CO.

4.2 Methods

4.2.1 Crystal synthesis

The synthesis was performed by Journey Byland, Peter Klavins, and Valentin Taufour. Single crystals of FeSe and $FeSe_{1-x}S_x$ were grown using the chemical vapor transport method in a tilted furnace following the methods outlined in [100]. Pure samples were characterized using a powder x-ray diffractometer. To determine the relationship between actual and nominal sulfur substitution levels, sulfur substituted samples were characterized using a Cameca SX-100 Electron Microprobe. Several platelets with dimensions between 1mm-2mm by 1mm-2mm were selected from each batch for characterization.

4.2.2 STM/S

STM/S measurements were performed by Morgan Walker, Zeke Zhao, Eduardo da Silva Neto, and myself using a customized Unisoku USM-1300 instrument. The samples were cleaved *in situ* in a ultra high vacuum environment with pressures below 10^{-9} Torr. All

STM/S measurements were done at 4.2 K and the differential conductance measurements (dI/dV) were performed using a lock-in technique.

Figure 4.1 shows real space images at $V = -30$ mV and QPI dispersions for three different sulfur concentrations, $x = 0.02, 0.14, 0.23$. The real space STS maps shown in Figures 4.1(a-c) were taken over a 256 x 256 grid and the black arrows indicate the direction of the b-axis. (a) was taken over an area of 132 nm x 132 nm with a bias setpoint of -50 mV, current setpoint of 200 pA, and modulation amplitude of 0.8 mV. (b) was taken over an area of 172 nm x 172 nm with a bias setpoint of -50 mV, current setpoint of 220 pA, and modulation amplitude of 1.5 mV. This measurement features a domain wall where the nematic direction rotates by 90 degrees. (c) was taken over an area of 172 nm x 172 nm with a bias setpoint of -42 mV, current setpoint of 270 pA and modulation amplitude of 1.5 mV.

The QPI dispersion maps (Figures 4.1(d-i) are line cuts of the Fourier transforms (FTs) of the real-space STS maps along the in-plane lattice directions where $a > b$ in the orhtorhombic state. (d) and (g) are a combination of two maps: the lower portion (-55 to -15 meV) is from the same data set as (a) with a bias step size of 1 mV and the upper portion (-14 to 45 meV) was taken over an area of 50 nm x 50 nm with a bias setpoint of -50 mV, current setpoint of 200 pA, bias step size of 2 mV and modulation amplitude of 1.6 mV. The map smaller in area was interpolated to match the Q-space and energy resolution of the larger map. (e) features the same data set as (b) and has a bias step size of 2 mV. (f-i) feature the same data set as (c) with a bias step size of 1.5 mV.

At the lowest doping, strong QPI patterns along Q_b are observed. Four distinct dispersive-bands can be identified below the FL and by comparing to ARPES they can be connected to particular scattering events on the Fermi surface. Along the Q_a direction, two non-dispersive features between the energy ranges of -40 to -30 meV and -15 to -5 meV at $Q = 0.1$ Å^{-1}

are observed. Above the FL an electron-like band is observed along Q_a, and the Q_b direction becomes dominated by a static feature near $Q_a = 0.1\,\text{Å}^{-1}$.

Beyond the nematic critical point, at $x = 0.23$, a pattern that is symmetric along the a and b directions is observed, as seen by the nearly identical QPI-bands shown in Figure 4.1(f) and (i). At $E = -30\,\text{meV}$, the real space dI/dV is considerably more disordered than what is observed at lower dopings within the nematic phase. The scattering centers are less obvious which could be related to the lack of unidirectional modulations. At and above the FL, a CDW-like pattern that does not disperse with energy is observed, which will be the focus of the following section.

4.2.3 ARPES

ARPES measurements were performed by Morgan Walker, Ryan Day, Eduardo da Silva Neto, and myself at the Quantum Materials Spectroscopy Centre beamline at the Canadian Light Source with the assistance of Seregy Gorovikov, Tor Pedersen, Sergey Zhdanovich, and Matteo Michiardi. Measurements were performed using both vertically and horizontally polarized photons with energy ranging from 18 to 40 eV (see figure captions). Samples were cleaved *in situ* and measured at pressure lower than 5×10^{-11} Torr and a temperature of 9 K. The combined beamline-analyzer (Scienta R4000) resolutions in angle and energy are better than 0.1° and 9 meV, respectively, for the combinations of beamline parameters (monochromator grating, exit slit temperature, photon energy) used.

4.3 Results

Figure 4.2(c) and (d) shows representative STM topographic images of the Se termination layers of the $x = 0$ and $x = 0.23$ samples, and their spatially averaged dI/dV spec-

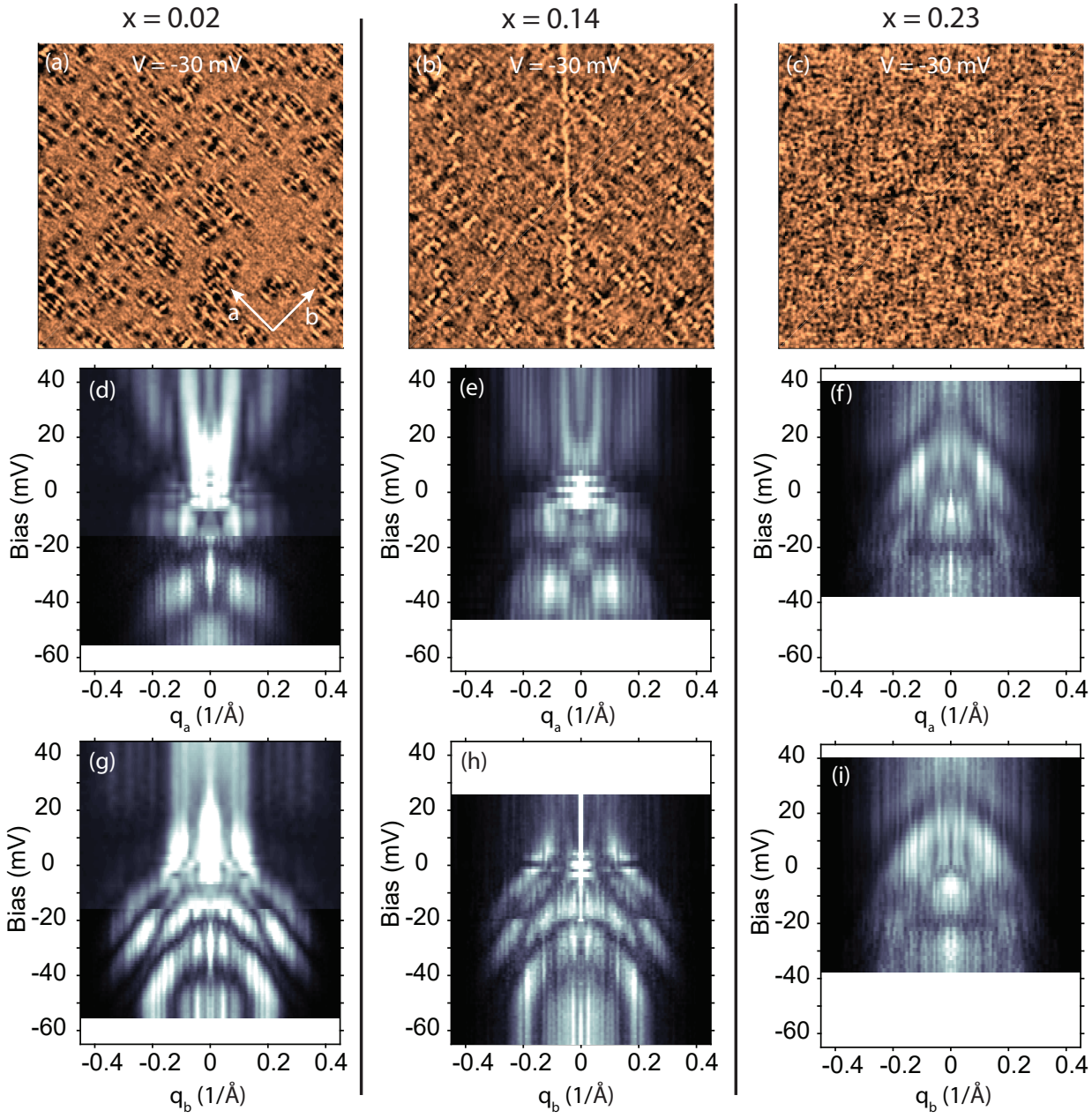

Figure 4.1: Sulfur-concentration dependence of QPI: (**a-c**) dI/dV maps at $V = -30\,\mathrm{mV}$ for three dopings: $x = 0.02, 0.140.23$. (**d-f**) QPI dispersions along q_a. (**g-i**) QPI dispersions along q_b. For the $x = 0.14$ data, the QPI dispersions were calculated over the left domain only.

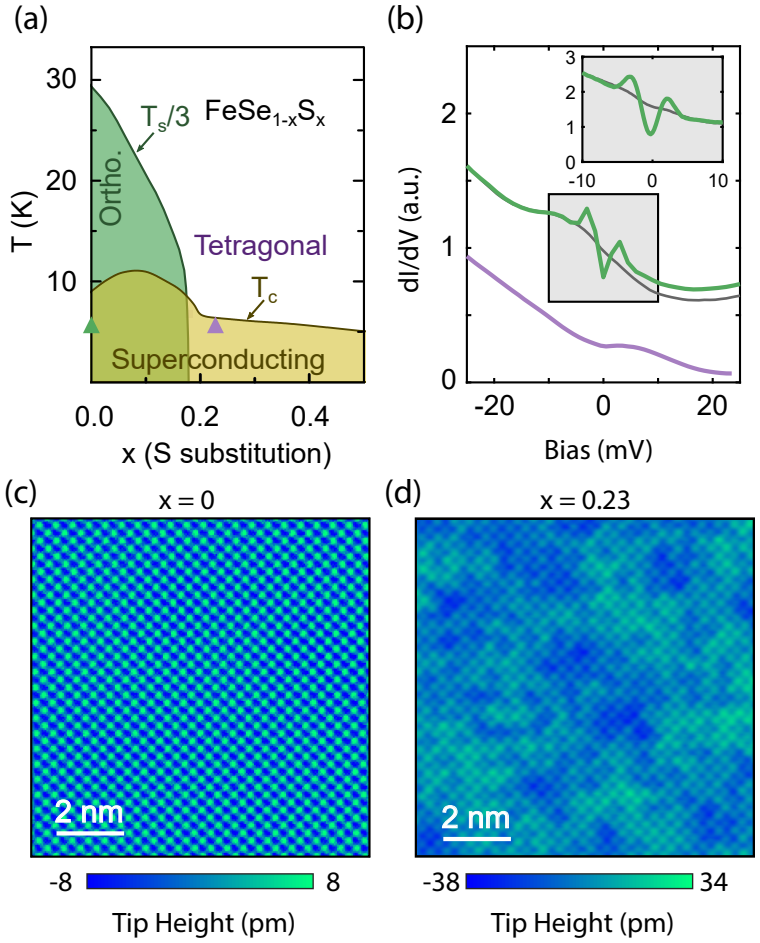

Figure 4.2: Phase diagrams, DOS, and topographies: (**a**) Phase diagram of $FeSe_{1-x}S_x$ based on [99], indicating the structural and superconducting transitions, T_S and T_c. For simplicity, we show the $T_S/3$ line. The two samples studied in this work ($x = 0$ and $x = 0.23$) were measured at 4.2 K, green and purple triangles, respectively. (**b**) Spatially averaged differential conductance (dI/dV) spectra of FeSe (green) and $FeSe_{0.77}S_{0.23}$ (purple). The grey curve is the spectrum of $FeSe_{0.98}S_{0.02}$ with a 10 T field applied normal to the a-b plane to suppress superconductivity. The inset shows two spectra with higher energy resolution in the range of the superconducting gap, taken on the same sample with no field applied (green) and under 10 T. (**c-d**) Constant current topographic images of FeSe and $FeSe_{0.77}S_{0.23}$ showing the atomically resolved (Se,S) termination layer.

tra. In the case of $FeSe_{0.77}S_{0.23}$, the S atoms appear in the topography as densely distributed C_4 symmetric features replacing the Se atoms, consistent with previous experiments [101, 102]. To investigate the symmetries of the electronic states in orthorhombic and tetragonal $FeSe_{1-x}S_x$, STS imaging was performed on $x = 0.14$ and $x = 0.23$ samples. Measurements of $FeSe_{0.86}S_{0.14}$ show two-fold symmetric modulations of the density of states (DOS), oriented along the smallest Fe-Fe distances (a and b), that are due to quasiparticle interference (QPI) near underlying Fe vacancies and reflect the C_2 symmetric band structure in the orthorhombic phase, Figures 4.3(a) and (b). The same images also show the presence of an orthorhombic domain wall, evidenced by the 90° rotated QPI patterns across the boundary. Fourier transforms (FTs) of the dI/dV patterns over a single domain (Figures 4.4(a) and (b)) confirm their C_2 symmetry at different energies. On the other hand, the FT patterns over a similar field of view in $FeSe_{0.77}S_{0.23}$ are C_4 symmetric (Figures 4.3(c) and (d)). This is consistent with this sample being tetragonal on average, although C_2 electronic patterns at smaller scales still exist as discussed later. Note that at $V = -36\,\mathrm{mV}$ the FT images show that well defined peaks in $FeSe_{0.86}S_{0.14}$ are replaced by a less intense and broader cross-like feature in $FeSe_{0.77}S_{0.23}$ (Figs. 4.4(c) and (d)). Of course, this is due to the scrambling of the spatial modulations caused by the random distribution of S atoms in $FeSe_{0.77}S_{0.23}$. Interestingly, the same effect is not observed at energies closer to the Fermi level. Instead, the FTs once again feature intense and sharp peaks at $|q_{a,b}| \approx 0.12\,\mathrm{\AA}^{-1}$ (Fig. 4.4(d)). While these peaks may resemble the QPI peaks in the FTs of FeSe, their underlying real-space patterns are starkly different. Whereas the QPI patterns in $FeSe_{0.86}S_{0.14}$ are clearly centered around the Fe vacancies, a similar correlation to impurities is not as clear in the data for $FeSe_{0.77}S_{0.23}$ in Fig. 4.3(d). Instead, those spatial modulations appear to more uniformly span the field of view, which suggests the existence of an incipient CO that breaks translational symmetry.

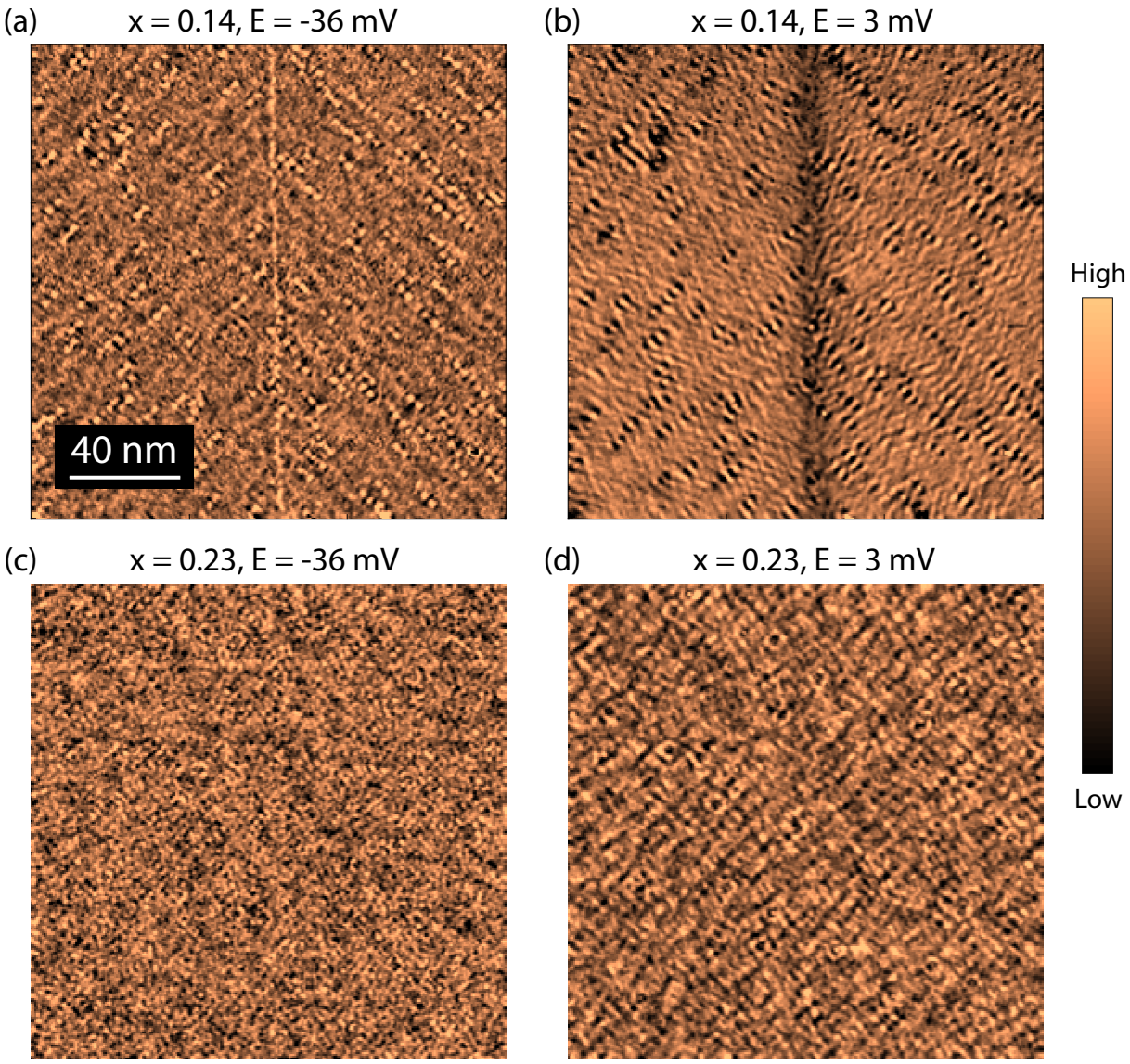

Figure 4.3: Real space QPI comparison: dI/dV maps at $V = -36\,\mathrm{mV}$ and $V = 3\,\mathrm{mV}$ for $x = 0.14$ and $x = 0.23$ samples. The orthorhombic samples ($x = 0.14$) feature a domain boundary that separates orthogonal nematic states.

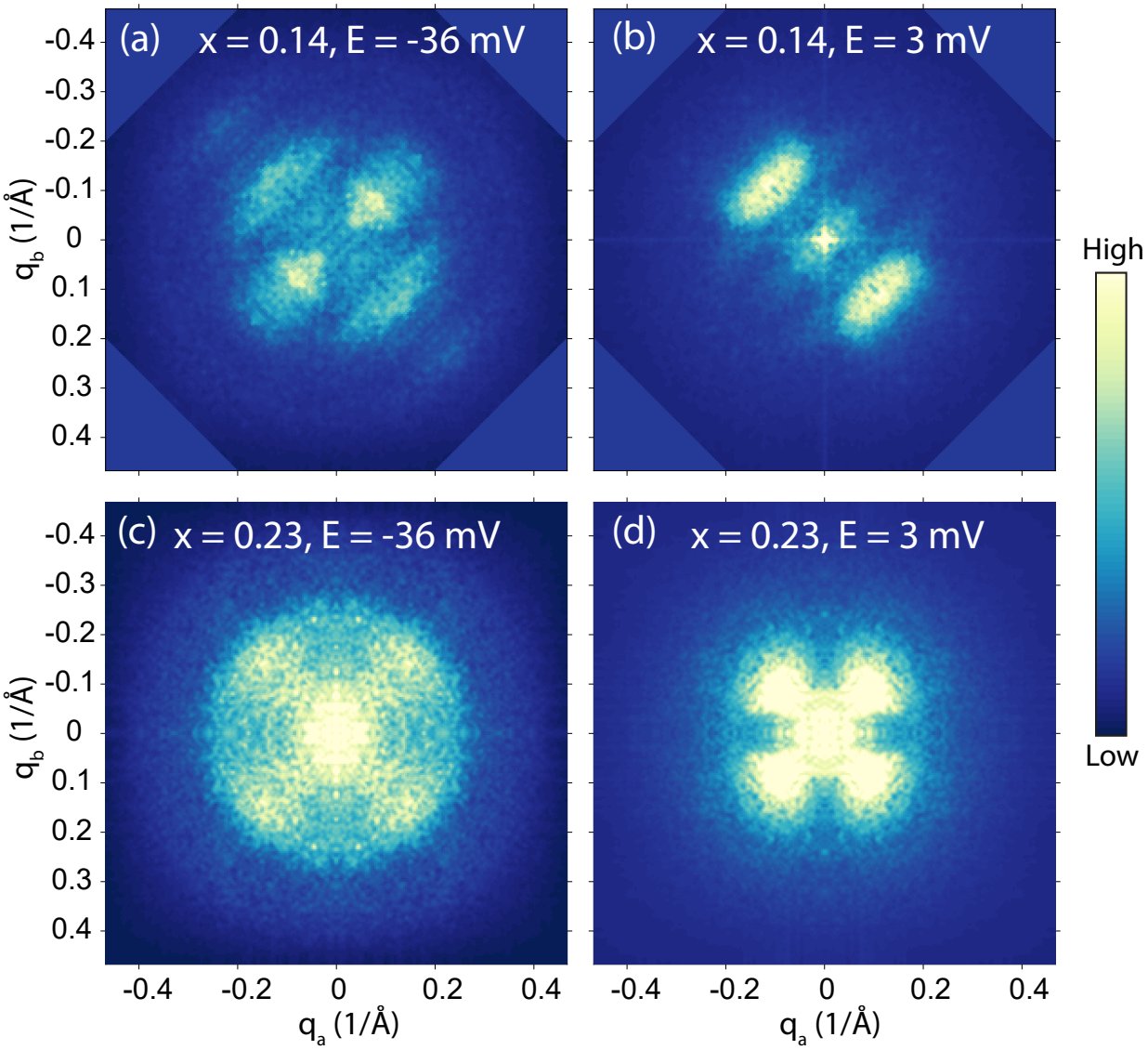

Figure 4.4: Q-space QPI comparison: FTs of dI/dV maps at $V = -36\,\mathrm{mV}$ and $V = 3\,\mathrm{mV}$ for $x = 0.14$ and $x = 0.23$ samples. The FTs display C_2 and C_4 symmetry, corresponding to the nematic and tetragonal phases.

The origin of the electronic patterns near the Fermi level in $FeSe_{0.77}S_{0.23}$can be identified from the energy dependence of the STS maps. Although both QPI and CO cause spatial modulations in dI/dV maps, the two phenomena have distinct behavior as a function of energy: the wavelength of the spatial modulations are energy-dependent in the case of QPI but independent of energy for CO [103]. A relevant example of this phenomenology occurs in the well established case of $Bi_2Sr_2CaCu_2O_{8+x}$ (Bi2212) [104]. Figure 4.5(a) shows a dI/dV map with periodic patterns along both Cu-O bond directions. Fourier analysis of the modulations along one of those directions shows two peaks with distinct energy trends: a dispersive feature associated with QPI (yellow line) and a non-dispersive peak originating from CO (red box) (Figure 4.5(b)). Remarkably, a similar analysis reveals the same phenomenology in $FeSe_{0.77}S_{0.23}$, Figures 4.6(a) and (b), indicating dispersive and non-dispersive charge modulations that overlap in momentum space. These two coexisting modulations can be disentangled by analyzing the spatially resolved tunneling current, $I(V)$, which is the integral of dI/dV from 0 to V and the ratio maps, $(dI/dV)/I$. While the $I(V)$ maps emphasize the non-dispersive peak at $q_{a,b} \approx 0.12\,\text{Å}^{-1}$ relative to the dispersive QPI, Figures 4.6(c) and (d), the ratio of dI/dV to $I(V)$ has the opposite effect, diminishing the effect of the non-dispersive component, Figures 4.6(e) and (f). Overall, the analysis above shows a striking similarity to the phenomenology in the cuprates, strongly indicating the presence of CO in $FeSe_{0.77}S_{0.23}$.

Theoretical calculations were performed by Jakob Böker, Marvin Müller, and Ilya Eremin, providing further evidence for the existence and origination of CO in $FeSe_{0.77}S_{0.23}$. In particular, using a low-energy model used to calculate the band structure in FeSe and $FeSe_{1-x}S_x$ [105, 106] was used to calculate the band structure and subsequent QPI patterns in $FeSe_{0.77}S_{0.23}$. Figures 4.7(a) and (b) show the calculated QPI patterns taking into account all possible inter- and intra-band scatterings at constant $k_z = \pi$ and $k_z = 0$, respec-

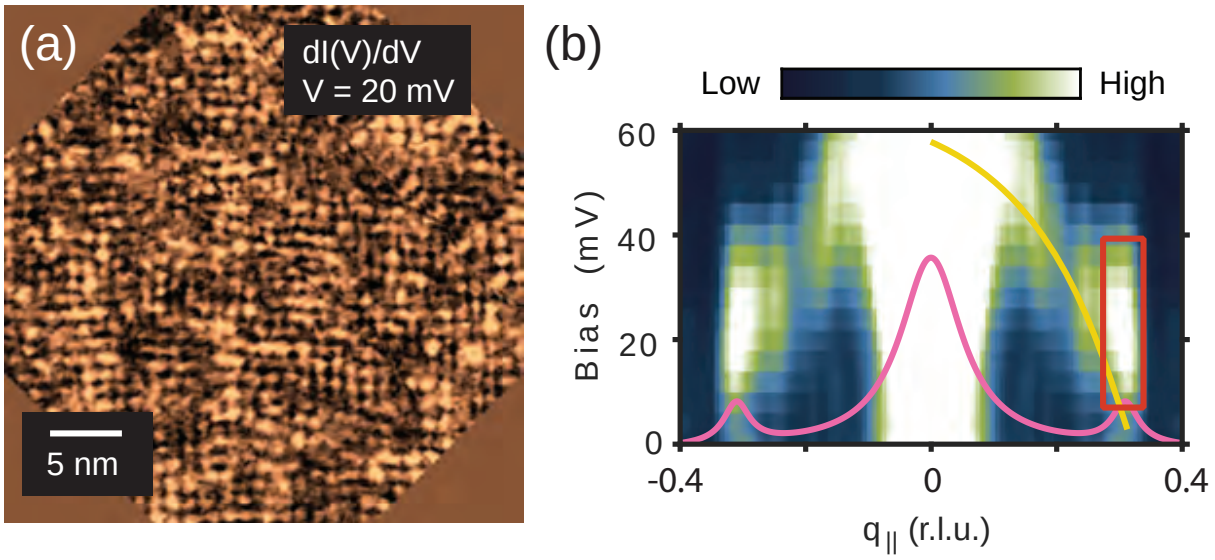

Figure 4.5: CO in $Bi_2Sr_2CaCu_2O_{8+x}$: (**a**) dI/dV map of a cuprate superconductor, $Bi_2Sr_2CaCu_2O_{8+x}$ at $V = 20\,\mathrm{mV}$. (**b**) Energy-momentum structure of the of the modulations obtained from the FTs of dI/dV measurements of $Bi_2Sr_2CaCu_2O_{8+x}$, with $q_{||}$ along the Cu-O bond direction. The magenta line in (b) the sum of the bias over $V = [0, 60]\,\mathrm{mV}$. The yellow lines highlight the dispersive QPI signal, while the red boxes emphasize the non-dispersive CO. The data was obtained from Ref. [104].

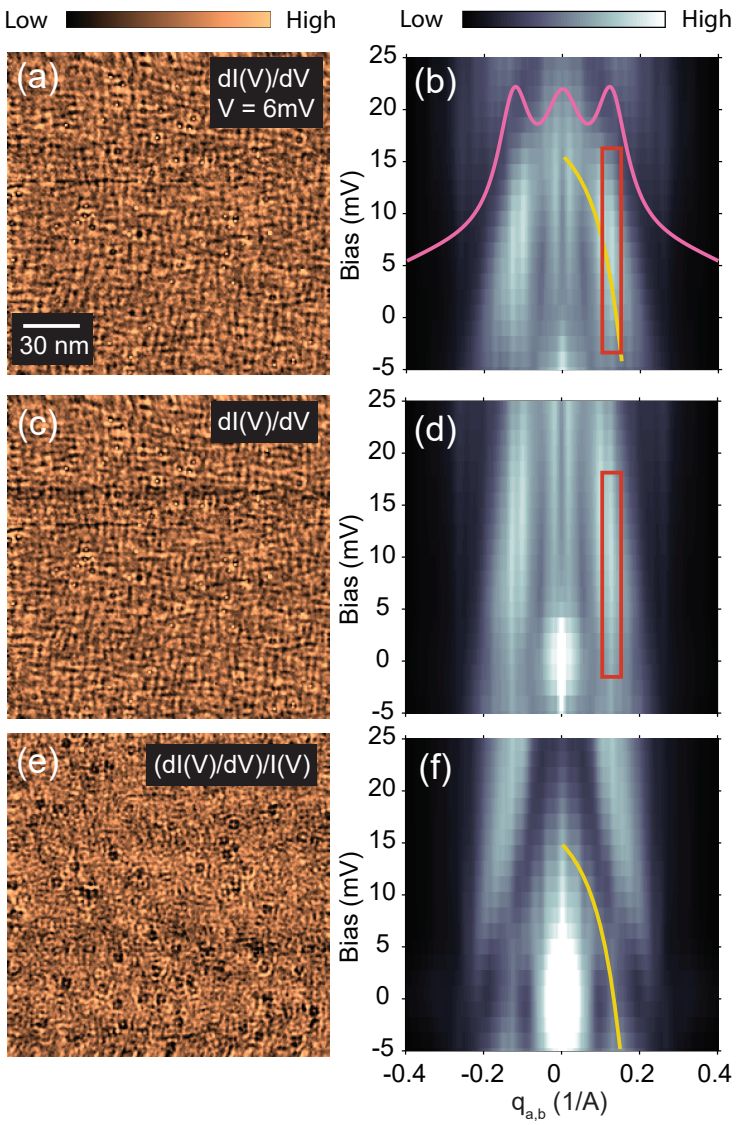

Figure 4.6: CO in $FeSe_{0.77}S_{0.23}$: (**a,c,e**) dI/dV, I, and $(dI/dV)/I$ maps of an $FeSe_{0.77}S_{0.23}$ sample measured at 6 mV, respectively. (**b,d,f**) Energy-momentum structure of the modulations along the smallest Fe-Fe direction, averaged over $[q_a = 0, q_b]$ and $[q_a, q_b = 0]$ directions, obtained from the FTs of (a), (c), and (e), respectively. The magenta line in (b) the sum of the bias over $V = [-5, 25]$ mV. The yellow lines highlight the dispersive QPI signal, while the red boxes emphasize the non-dispersive CO.

tively. The three hole-like dispersive features observed in the STS data are well accounted for in the calculations, see Figures 4.7(c). Note that the calculations reproduce the experimentally determined QPI even for the unoccupied states where ARPES is not an input to the model, which further validates the calculated band structure. Of course, the calculations show QPI features that are not present in the experimental data and a more realistic model would have to take into account matrix-element effects and orbital selective correlations to properly account for some of the forbidden scattering. Still, even with all possible scattering channels included in the calculations, a non-dispersive feature is never present, thus further ruling out a QPI origin for the dispersionless feature observed in the STS data. More importantly, the absence in the calculations of any strong features near $q_{a,b} \approx 0.12\,\text{Å}^{-1}$ at the Fermi level demonstrates that the CO in $FeSe_{0.77}S_{0.23}$ is not caused by Fermi surface nesting, likely leaving strong correlations as its origin.

4.4 Discussion

Altogether, the STM/S data, ARPES experiments, and theoretical modeling establish the presence of CO in $FeSe_{0.77}S_{0.23}$. A further analysis of the STS images allows for investigation of the local rotational symmetry of the CO. Figure 4.8(a), shows a dI/dV map of the CO, which can be separated into two regions (red and blue) whose individual FTs show $0.12\,\text{Å}^{-1}$ modulations only along a or only along b. This dichotomy is more evident in the filtered image shown in Fig. 4.8(b), which shows that the CO emerges as alternating domains of stripes. Stripe-like modulations in IBSCs with different periods and coherence lengths have been reported by STM/S in two other situations: LiFeAs under external uniaxial stress [107] and ultrathin (one and two monolayers) FeSe films on $SrTiO_3$ [108, 109]. However, in those two cases the underlying crystal structure already breaks rotational symmetry, indicating that a

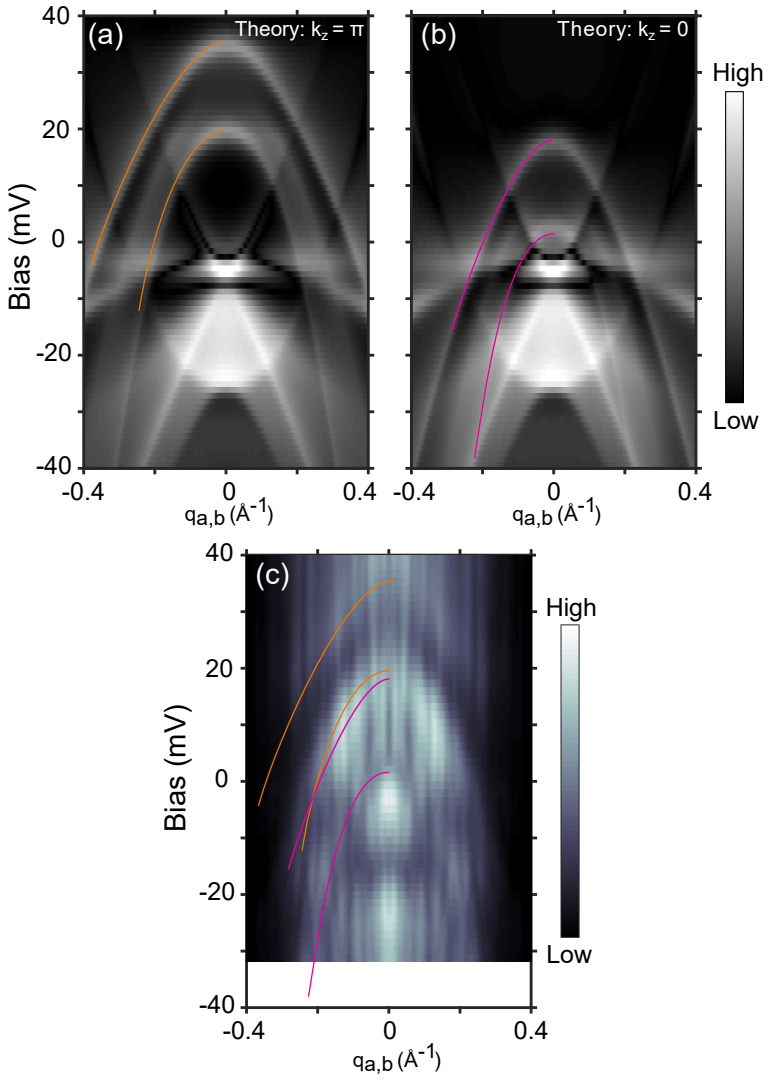

Figure 4.7: Theoretical QPI calculations: (**a**-**b**) Energy-momentum structure of the modulations along the smallest Fe-Fe direction, $(q_a, q_b = 0)$ (a and b equivalent in the tetragonal structure) calculated from a band structure model fitted to ARPES data for $k_z = \pi$ and $k_z = 0$. (**c**) dI/dV measurements and averaged over $[q_a = 0, q_b]$ and $[q_a, q_b = 0]$ directions. Orange and pink lines are guides to the eye.

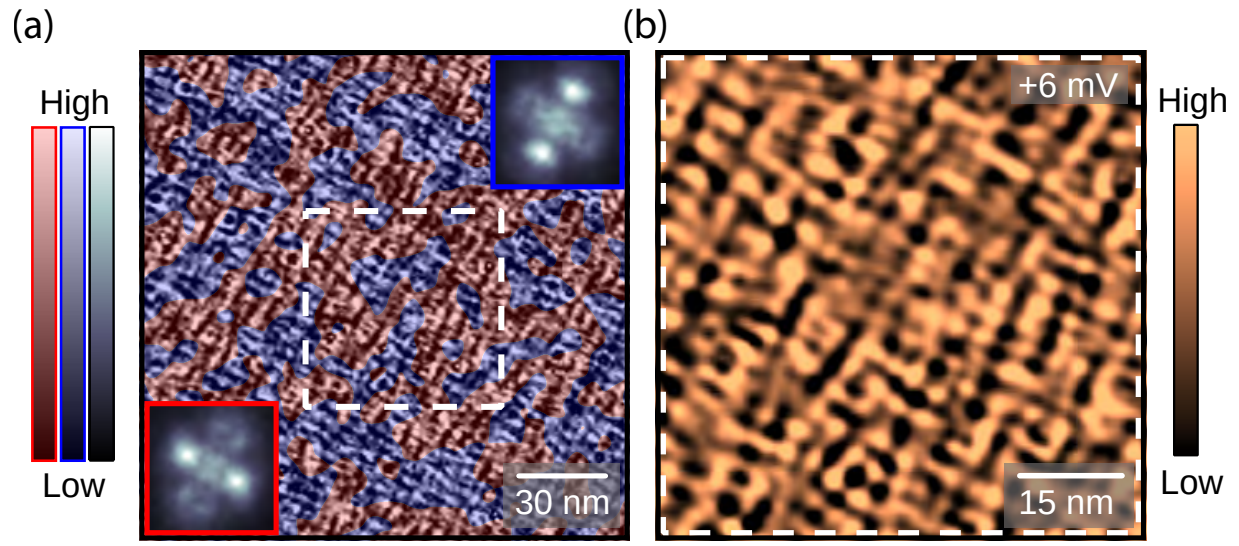

Figure 4.8: Local nematicity of CO: (**a**) dI/dV map measured on a $FeSe_{0.77}S_{0.23}$ sample at 6 mV. The image is overlaid with red and blue transparent masks that indicate regions of CO only along a or only along b. The insets show the FTs over the two distinct regions under the red and blue masks. (**b**) Zoom in of the region delimited by the dashed lines in **a**, with the image filtered to highlight the local structure of the CO.

C_2 symmetric lattice may be necessary to foster the formation of the stripes. Instead, the STS data on $FeSe_{0.77}S_{0.23}$ reveals an incipient C_2 symmetric CO that is likely electronically driven given that it is present in the tetragonal sample, but not the orthorhombic sample. Additionally, this stripe-like CO likely influences the other electronic phases of $FeSe_{1-x}S_x$. For example, noting that nematic correlations are known to persist throughout the phase diagram of $FeSe_{1-x}S_x$, even deep into the tetragonal phase [98, 110, 111], one would expect that their C_2 symmetry allows them to easily couple to the unidirectional CO. One may also reasonably expect that CO also couples to magnetic correlations and superconductivity, directly or indirectly (via nematic correlations), and is therefore a key ingredient to understanding the phase diagram of $FeSe_{1-x}S_x$.

The discovery of CO in $FeSe_{0.77}S_{0.23}$ raises new interesting questions regarding its influence on superconductivity. For example, the drop of T_c and the change of the superconducting gap across x_c [102] may be related to a competition between CO and superconductivity, similar to what is observed in cuprates [84]. Furthermore, in the scenario where nematic fluctuations participate in the superconducting pairing, the presence of CO could have an adverse effect to superconductivity by pinning dynamic nematic correlations into static short-range puddles. Additionally, the same type of pinning may explain why quantum critical behavior appears to not be fully realized down to low temperatures near x_c, as suggested by quantum oscillations [99, 112]and by the deviation from Curie-Weiss behavior in elastoresistance measurements [98]. Finally, the results provide two important clues suggesting that the CO in $FeSe_{1-x}S_x$ emerges from orbital-selective strong electron correlations: *(i)* a Fermi surface instability or nesting scenario is ruled out and *(ii)* the CO appears over a specific energy range, approximately -5 to 25 meV. Whether these are the same correlations responsible for the low quasiparticle weight of the d_{xy} and d_{xz} orbitals near the Fermi level and the orbital-selective Cooper pairing in FeSe [95, 96] requires further investigations. Clearly, there is still much to be understood about the CO uncovered by this study and experimental answers to the above questions, and others, will require detailed studies as a function of S concentration and temperature. Nevertheless, these experiments firmly establish unidirectional CO as a critical component for understanding nematicity and superconductivity in $FeSe_{1-x}S_x$.

Chapter 5

Summary

Topological surface states above the Fermi level in Hf_2Te_2P were resolved using STS and ARPES. The results establish that the material possesses both weak and strong topological insulator states. By tuning the Fermi level via chemical doping or a gate voltage, one may be able to control the conductivity on the material's surface between insulating and dissipationless states, which could be used in the development of switchable electronic devices [7].

The RXS experiments on $La_{1.475}Nd_{0.4}Sr_{0.125}CuO_4$ under uniaxial stress provide new insight into the relationship between the charge stripes and low-temperature structural transition, establishing stress as a powerful tool to control the phase transitions of the material. Given the strong relationship between stress and superconductivity, the study shows the potential for uniaxial stress to be used as a tuning parameter to easily alter material's electronic properties. Further studies that are able to apply uniaxial stress in situ should be performed to determine how the transition temperatures change as a function of stress. Additionally, in situ stress would allow for measurements of the effects of stress on the high-temperature charge order correlations [18].

The observation of CO in $FeSe_{0.77}S_{0.23}$ raises several questions about the role of orbital-selective electronic correlations and the origin of superconductivity in the IBSCs. While the results on this specific composition have revealed the charge order state in the tetragonal phase, measurements should be performed above the nematic transition temperature on samples that exhibit the nematic state to determine the role of charge order in the development of electronic nematicity and superconductivity. Additionally, resonant x-ray scattering experiments should be performed to determine the bulk properties of the charge order.

These studies only scratch the surface of the numersous interesting electronic properties found in topological materials and superconductors. Finding practical ways to utilize their properties such as dissipationless transport is the ultimate goal and requires studies such as these that uncover the fundamental properties of the materials and phases. With advancements in experimental instrumentation, crystal synthesis techniques, and theoretical modeling, condensed matter physics will continue to offer fascinating insights into the material world and usher in the next generation of technological breakthroughs.

Bibliography

[1] L. D. Landau. On the theory of phase transitions. *Zh. Eksp. Teor. Fiz.*, 7:19–32, 1937.

[2] Piers Coleman. *Introduction to Many-Body Physics*. Cambridge University Press, 2015. doi: 10.1017/CBO9781139020916.

[3] James P. Sethna. *Lectures in the Sciences of Complexity*. Addison-Wesley Publishing Compnay, Inc., 1992.

[4] Pedram Roushan, Jungpil Seo, Colin V. Parker, Y. S. Hor, D. Hsieh, Dong Qian, Anthony Richardella, M. Z. Hasan, R. J. Cava, and Ali Yazdani. Topological surface states protected from backscattering by chiral spin texture. *Nature*, 460:1106, August 2009.

[5] C. L. Kane and E. J. Mele. Z_2 topological order and the quantum spin hall effect. *Phys. Rev. Lett.*, 95:146802, Sep 2005. doi: 10.1103/PhysRevLett.95.146802.

[6] Yoichi Ando. Topological insulator materials. *Journal of the Physical Society of Japan*, 82(10):102001, 2013. doi: 10.7566/JPSJ.82.102001.

[7] T. J. Boyle, A. Rossi, M. Walker, P. Carlson, M. K. Miller, J. Zhao, P. Klavins, C. Jozwiak, A. Bostwick, E. Rotenberg, V. Taufour, I. M. Vishik, and E. H. da Silva Neto. Topological surface states above the fermi level in hf_2te_2P. *Phys. Rev. B*, 100:081105, Aug 2019. doi: 10.1103/PhysRevB.100.081105.

[8] J. Bardeen, L. N. Cooper, and J. R. Schrieffer. Theory of superconductivity. *Phys. Rev.*, 108:1175–1204, Dec 1957. doi: 10.1103/PhysRev.108.1175.

[9] Michael R. Norman. The challenge of unconventional superconductivity. *Science*, 332 (6026):196–200, 2011. doi: 10.1126/science.1200181.

[10] G. R. Stewart. Unconventional superconductivity. *Advances in Physics*, 66(2):75–196, 2017. doi: 10.1080/00018732.2017.1331615.

[11] M. K. Wu, J. R. Ashburn, C. J. Torng, P. H. Hor, R. L. Meng, L. Gao, Z. J. Huang, Y. Q. Wang, and C. W. Chu. Superconductivity at 93 k in a new mixed-phase y-ba-cu-o compound system at ambient pressure. *Phys. Rev. Lett.*, 58:908–910, Mar 1987. doi: 10.1103/PhysRevLett.58.908. URL https://link.aps.org/doi/10.1103/PhysRevLett.58.908.

[12] A Schilling, M Cantoni, J D Guo, and H R Ott. Superconductivity above 130 K in the Hg–Ba–Ca–Cu–O system. *Nature*, 363(6424):56–58, 1993. ISSN 1476-4687. doi: 10.1038/363056a0. URL https://doi.org/10.1038/363056a0.

[13] G. Ghiringhelli, M. Le Tacon, M. Minola, S. Blanco-Canosa, C. Mazzoli, N. B. Brookes, G. M. De Luca, A. Frano, D. G. Hawthorn, F. He, T. Loew, M. Moretti Sala, D. C. Peets, M. Salluzzo, E. Schierle, R. Sutarto, G. A. Sawatzky, E. Weschke, B. Keimer, and L. Braicovich. Long-range incommensurate charge fluctuations in (Y,Nd)$Ba_2Cu_3O_{6+x}$. 337(6096):821–825, 2012. ISSN 0036-8075. doi: 10.1126/science.1223532.

[14] J. Chang, E. Blackburn, A. T. Holmes, N. B. Christensen, J. Larsen, J. Mesot, Ruixing Liang, D. A. Bonn, W. N. Hardy, A. Watenphul, M. v. Zimmermann, E. M. Forgan, and S. M. Hayden. Direct observation of competition between superconductivity and charge density wave order in $YBa_2Cu_3O_{6.67}$. *Nature Physics*, 8(12):871–876, Dec 2012. ISSN 1745-2481. doi: 10.1038/nphys2456.

[15] Eduardo H. da Silva Neto, Pegor Aynajian, Alex Frano, Riccardo Comin, Enrico Schierle, Eugen Weschke, András Gyenis, Jinsheng Wen, John Schneeloch, Zhijun Xu, Shimpei Ono, Genda Gu, Mathieu Le Tacon, and Ali Yazdani. Ubiquitous interplay between charge ordering and high-temperature superconductivity in cuprates. 343(6169):393–396, 2014. ISSN 0036-8075. doi: 10.1126/science.1243479.

[16] Mirela Dragomir, Qianli Ma, J. Patrick Clancy, Amirreza Ataei, Paul A. Dube, Sudarshan Sharma, Ashfia Huq, Hanna A. Dabkowska, Louis Taillefer, and Bruce D. Gaulin. Materials preparation, single-crystal growth, and the phase diagram of the cuprate high-temperature superconductor $la_{1.6-x}nd_{0.4}sr_xCuo_4$. *Phys. Rev. Materials*, 4:114801, Nov 2020. doi: 10.1103/PhysRevMaterials.4.114801.

[17] Naman K. Gupta, Christopher McMahon, Ronny Sutarto, Tianyu Shi, Rantong Gong, Haofei I. Wei, Kyle M. Shen, Feizhou He, Qianli Ma, Mirela Dragomir, Bruce D. Gaulin, and David G. Hawthorn. Vanishing nematic order beyond the pseudogap phase in overdoped cuprate superconductors. 118(34), 2021. ISSN 0027-8424. doi: 10.1073/pnas.2106881118.

[18] T. J. Boyle, M. Walker, A. Ruiz, E. Schierle, Z. Zhao, F. Boschini, R. Sutarto, T. D. Boyko, W. Moore, N. Tamura, F. He, E. Weschke, A. Gozar, W. Peng, A. C. Komarek,

A. Damascelli, C. Schüßler-Langeheine, A. Frano, E. H. da Silva Neto, and S. Blanco-Canosa. Large response of charge stripes to uniaxial stress in $la_{1.475}nd_{0.4}sr_{0.125}cuo_4$. *Phys. Rev. Research*, 3:L022004, Apr 2021. doi: 10.1103/PhysRevResearch.3.L022004.

[19] Davis Baird and Ashley Shew. Probing the history of scanning tunneling microscopy. *Discovering the Nanoscale*, 01 2004.

[20] C Julian Chen. *Introduction to Scanning Tunneling Microscopy: Second Edition*. Oxford University Press, Oxford. ISBN 9780199211500. doi: 10.1093/acprof:oso/9780199211500.001.0001.

[21] Jennifer E Hoffman. Spectroscopic scanning tunneling microscopy insights into fe-based superconductors. *Reports on Progress in Physics*, 74(12):124513, nov 2011. doi: 10.1088/0034-4885/74/12/124513. URL https://doi.org/10.1088/0034-4885/74/12/124513.

[22] Riccardo Comin and Andrea Damascelli. Resonant x-ray scattering studies of charge order in cuprates. *Annual Review of Condensed Matter Physics*, 7(1):369–405, 2016. doi: 10.1146/annurev-conmatphys-031115-011401.

[23] Xiao-Liang Qi and Shou-Cheng Zhang. Topological insulators and superconductors. *Rev. Mod. Phys.*, 83:1057–1110, Oct 2011. doi: 10.1103/RevModPhys.83.1057.

[24] M. Z. Hasan and C. L. Kane. Colloquium: Topological insulators. *Rev. Mod. Phys.*, 82:3045–3067, Nov 2010. doi: 10.1103/RevModPhys.82.3045.

[25] N. P. Armitage, E. J. Mele, and Ashvin Vishwanath. Weyl and dirac semimetals in three-dimensional solids. *Rev. Mod. Phys.*, 90:015001, Jan 2018. doi: 10.1103/RevModPhys.90.015001.

[26] Shuo-Ying Yang, Hao Yang, Elena Derunova, Stuart S. P. Parkin, Binghai Yan, and Mazhar N. Ali. Symmetry demanded topological nodal-line materials. *Advances in Physics: X*, 3(1):1414631, 2018. doi: 10.1080/23746149.2017.1414631.

[27] Jason Alicea. New directions in the pursuit of majorana fermions in solid state systems. *Reports on Progress in Physics*, 75(7):076501, jun 2012. doi: 10.1088/0034-4885/75/7/076501. URL https://doi.org/10.1088%2F0034-4885%2F75%2F7%2F076501.

[28] Libor Šmejkal, Yuriy Mokrousov, Binghai Yan, and Allan H MacDonald. Topological antiferromagnetic spintronics. *Nature Physics*, (3):242–251. ISSN 1745-2481. doi: 10.1038/s41567-018-0064-5.

[29] Huiwen Ji, I. Pletikosić, Q. D. Gibson, Girija Sahasrabudhe, T. Valla, and R. J. Cava. Strong topological metal material with multiple dirac cones. *Phys. Rev. B*, 93:045315, Jan 2016. doi: 10.1103/PhysRevB.93.045315.

[30] Md Mofazzel Hosen, Klauss Dimitri, Ashis Kumar Nandy, Alex Aperis, Raman Sankar, Gyanendra Dhakal, Pablo Maldonado, Firoza Kabir, Christopher Sims, F Chou, Dariusz Kaczorowski, Tomasz Durakiewicz, Peter Oppeneer, and Madhab Neupane. Distinct multiple fermionic states in a single topological metal. *Nature Communications*, 9:3002, 08 2018. doi: 10.1038/s41467-018-05233-1.

[31] Liang Fu and C. L. Kane. Topological insulators with inversion symmetry. *Phys. Rev. B*, 76:045302, Jul 2007. doi: 10.1103/PhysRevB.76.045302.

[32] Ming Yang and Wu-Ming Liu. The d-p band-inversion topological insulator in bismuth-based skutterudites. *Scientific Reports*, 4:5131, May 2014.

[33] J. E. Hoffman, K. McElroy, D.-H. Lee, K. M Lang, H. Eisaki, S. Uchida, and J. C. Davis. Imaging quasiparticle interference in bi2sr2cacu2o8+. 297(5584):1148–1151, 2002. ISSN 0036-8075. doi: 10.1126/science.1072640.

[34] Qiang-Hua Wang and Dung-Hai Lee. Quasiparticle scattering interference in high-temperature superconductors. *Phys. Rev. B*, 67:020511(R), Jan 2003. doi: 10.1103/PhysRevB.67.020511.

[35] Ilija Zeljkovic, Yoshinori Okada, Cheng-Yi Huang, R. Sankar, Daniel Walkup, Wenwen Zhou, Maksym Serbyn, Fangcheng Chou, Wei-Feng Tsai, Hsin Lin, A. Bansil, Liang Fu, M. Zahid Hasan, and Vidya Madhavan. Mapping the unconventional orbital texture in topological crystalline insulators. *Nature Physics*, 10:572, July 2014.

[36] Ali Yazdani, Eduardo H. da Silva Neto, and Pegor Aynajian. Spectroscopic imaging of strongly correlated electronic states. *Annual Review of Condensed Matter Physics*, 7(1):11–33, 2016. doi: 10.1146/annurev-conmatphys-031214-014529.

[37] Hiroyuki Inoue, András Gyenis, Zhijun Wang, Jian Li, Seong Woo Oh, Shan Jiang, Ni Ni, B. Andrei Bernevig, and Ali Yazdani. Quasiparticle interference of the fermi arcs and surface-bulk connectivity of a weyl semimetal. 351(6278):1184–1187, 2016. ISSN 0036-8075. doi: 10.1126/science.aad8766.

[38] Hao Zheng, Su-Yang Xu, Guang Bian, Cheng Guo, Guoqing Chang, Daniel S Sanchez, Ilya Belopolski, Chi-Cheng Lee, Shin-Ming Huang, Xiao Zhang, Raman Sankar, Nasser Alidoust, Tay-Rong Chang, Fan Wu, Titus Neupert, Fangcheng Chou, Horng-Tay Jeng, Nan Yao, Arun Bansil, Shuang Jia, Hsin Lin, and M Zahid Hasan. Atomic-Scale Visualization of Quantum Interference on a Weyl Semimetal Surface by Scanning Tunneling Microscopy. *ACS Nano*, (1):1378–1385, jan . ISSN 1936-0851. doi: 10.1021/acsnano.5b06807.

[39] Zhen Zhu, Tay-Rong Chang, Cheng-Yi Huang, Haiyang Pan, Xiao-Ang Nie, Xin-Zhe Wang, Zhe-Ting Jin, Su-Yang Xu, Shin-Ming Huang, Dan-Dan Guan, Shiyong Wang,

Yao-Yi Li, Canhua Liu, Dong Qian, Wei Ku, Fengqi Song, Hsin Lin, Hao Zheng, and Jin-Feng Jia. Quasiparticle interference and nonsymmorphic effect on a floating band surface state of ZrSiSe. *Nature Communications*, (1):4153. ISSN 2041-1723. doi: 10.1038/s41467-018-06661-9.

[40] Kristina Tschulik, Michael Ruck, Michael Binnewies, Edgar Milke, Stefan Hoffmann, Walter Schnelle, Boniface P. T. Fokwa, Michael Gilleßen, and Peer Schmidt. Chemistry and physical properties of the phosphide telluride zr2pte2. *European Journal of Inorganic Chemistry*, 2009(21):3102–3110. doi: 10.1002/ejic.200900346.

[41] K-W Chen, S Das, D Rhodes, S Memaran, T Besara, T Siegrist, E Manousakis, L Balicas, and R E Baumbach. Uncovering the behavior of hf2te2p and the candidate dirac metal zr2te2p. *Journal of Physics: Condensed Matter*, 28(14):14LT01, mar 2016. doi: 10.1088/0953-8984/28/14/14lt01. URL https://doi.org/10.1088%2F0953-8984%2F28%2F14%2F14lt01.

[42] M A Hossain, J D F Mottershead, D Fournier, A Bostwick, J L McChesney, E Rotenberg, R Liang, W N Hardy, G A Sawatzky, I S Elfimov, D A Bonn, and A Damascelli. In situ doping control of the surface of high-temperature superconductors. *Nature Physics*, page 527, jun .

[43] D Hsieh, L Wray, D Qian, Y Xia, J H Dil, F Meier, L Patthey, J Osterwalder, G Bihlmayer, Y S Hor, R J Cava, and M Z Hasan. Direct observation of spin-polarized surface states in the parent compound of a topological insulator using spin- and angle-resolved photoemission spectroscopy in a mott-polarimetry mode. *New Journal of Physics*, 12(12):125001, dec 2010. doi: 10.1088/1367-2630/12/12/125001. URL https://doi.org/10.1088%2F1367-2630%2F12%2F12%2F125001.

[44] Jungpil Seo, Pedram Roushan, Haim Beidenkopf, Y. S. Hor, R. J. Cava, and Ali Yazdani. Transmission of topological surface states through surface barriers. *Nature*, 466:343, July 2010.

[45] B. Keimer, S. A. Kivelson, M. R. Norman, S. Uchida, and J. Zaanen. From quantum matter to high-temperature superconductivity in copper oxides. *Nature*, 518(7538): 179–186, Feb 2015. ISSN 1476-4687. doi: 10.1038/nature14165.

[46] Eduardo Fradkin, Steven A. Kivelson, and John M. Tranquada. Colloquium: Theory of intertwined orders in high temperature superconductors. *Rev. Mod. Phys.*, 87:457–482, May 2015. doi: 10.1103/RevModPhys.87.457.

[47] Eduardo Fradkin, Steven A. Kivelson, Michael J. Lawler, James P. Eisenstein, and Andrew P. Mackenzie. Nematic fermi fluids in condensed matter physics. *Annual Review of Condensed Matter Physics*, 1(1):153–178, 2010. doi: 10.1146/annurev-conmatphys-070909-103925.

[48] J. M. Tranquada, B. J. Sternlieb, J. D. Axe, Y. Nakamura, and S. Uchida. Evidence for stripe correlations of spins and holes in copper oxide superconductors. *Nature*, 375 (6532):561–563, Jun 1995. ISSN 1476-4687. doi: 10.1038/375561a0.

[49] Jörg Fink, Enrico Schierle, Eugen Weschke, Jochen Geck, David Hawthorn, Viktor Soltwisch, Hiroki Wadati, Hsueh-Hung Wu, Hermann A. Dürr, Nadja Wizent, Bernd Büchner, and George A. Sawatzky. Charge ordering in $La_{1.8-x}Eu_{0.2}Sr_xCuO_4$ studied by resonant soft x-ray diffraction. *Phys. Rev. B*, 79:100502, Mar 2009. doi: 10.1103/PhysRevB.79.100502.

[50] M. Hücker, M. v. Zimmermann, G. D. Gu, Z. J. Xu, J. S. Wen, Guangyong Xu, H. J. Kang, A. Zheludev, and J. M. Tranquada. Stripe order in superconducting $La_{2-x}Ba_xCuO_4$ ($0.095 \leqslant x \leqslant 0.155$). *Phys. Rev. B*, 83:104506, Mar 2011. doi: 10.1103/PhysRevB.83.104506.

[51] Q. Li, M. Hücker, G. D. Gu, A. M. Tsvelik, and J. M. Tranquada. Two-dimensional superconducting fluctuations in stripe-ordered $La_{1.875}Ba_{0.125}CuO_4$. *Phys. Rev. Lett.*, 99:067001, Aug 2007. doi: 10.1103/PhysRevLett.99.067001.

[52] J. M. Tranquada, G. D. Gu, M. Hücker, Q. Jie, H.-J. Kang, R. Klingeler, Q. Li, N. Tristan, J. S. Wen, G. Y. Xu, Z. J. Xu, J. Zhou, and M. v. Zimmermann. Evidence for unusual superconducting correlations coexisting with stripe order in $La_{1.875}Ba_{0.125}CuO_4$. *Phys. Rev. B*, 78:174529, Nov 2008. doi: 10.1103/PhysRevB.78.174529.

[53] S. Blanco-Canosa, A. Frano, T. Loew, Y. Lu, J. Porras, G. Ghiringhelli, M. Minola, C. Mazzoli, L. Braicovich, E. Schierle, E. Weschke, M. Le Tacon, and B. Keimer. Momentum-dependent charge correlations in $YBa_2Cu_3O_{6+\delta}$ superconductors probed by resonant x-ray scattering: Evidence for three competing phases. *Phys. Rev. Lett.*, 110:187001, May 2013. doi: 10.1103/PhysRevLett.110.187001.

[54] K. Yamada, C. H. Lee, K. Kurahashi, J. Wada, S. Wakimoto, S. Ueki, H. Kimura, Y. Endoh, S. Hosoya, G. Shirane, R. J. Birgeneau, M. Greven, M. A. Kastner, and Y. J. Kim. Doping dependence of the spatially modulated dynamical spin correlations and the superconducting-transition temperature in $La_{2-x}Sr_xCuO_4$. *Phys. Rev. B*, 57: 6165–6172, Mar 1998. doi: 10.1103/PhysRevB.57.6165.

[55] A Lanzara, Guo meng Zhao, N L Saini, A Bianconi, K Conder, H Keller, and K A Müller. Oxygen-isotope shift of the charge-stripe ordering temperature in $La_{2-x}Sr_xCuO_4$ from x-ray absorption spectroscopy. *Journal of Physics: Condensed Matter*, 11(48):L541–L546, nov 1999. doi: 10.1088/0953-8984/11/48/103. URL https://doi.org/10.1088/0953-8984/11/48/103.

[56] O. Cyr-Choinière, D. LeBoeuf, S. Badoux, S. Dufour-Beauséjour, D. A. Bonn, W. N. Hardy, R. Liang, D. Graf, N. Doiron-Leyraud, and Louis Taillefer. Sensitivity of T_c to pressure and magnetic field in the cuprate superconductor $YBa_2Cu_3O_y$: Evidence of charge-order suppression by pressure. *Phys. Rev. B*, 98:064513, Aug 2018. doi: 10.1103/PhysRevB.98.064513.

[57] M. Hücker, M. v. Zimmermann, M. Debessai, J. S. Schilling, J. M. Tranquada, and G. D. Gu. Spontaneous symmetry breaking by charge stripes in the high pressure phase of superconducting $La_{1.875}Ba_{0.125}CuO_4$. *Phys. Rev. Lett.*, 104:057004, Feb 2010. doi: 10.1103/PhysRevLett.104.057004.

[58] H.-H. Kim, S. M. Souliou, M. E. Barber, E. Lefrançois, M. Minola, M. Tortora, R. Heid, N. Nandi, R. A. Borzi, G. Garbarino, A. Bosak, J. Porras, T. Loew, M. König, P. J. W. Moll, A. P. Mackenzie, B. Keimer, C. W. Hicks, and M. Le Tacon. Uniaxial pressure control of competing orders in a high-temperature superconductor. 362(6418):1040–1044, 2018. ISSN 0036-8075. doi: 10.1126/science.aat4708.

[59] H.-H. Kim, E. Lefrançois, K. Kummer, R. Fumagalli, N. B. Brookes, D. Betto, S. Nakata, M. Tortora, J. Porras, T. Loew, M. E. Barber, L. Braicovich, A. P. Mackenzie, C. W. Hicks, B. Keimer, M. Minola, and M. Le Tacon. Charge density waves in $YBa_2Cu_3O_{6.67}$ probed by resonant x-ray scattering under uniaxial compression. *Phys. Rev. Lett.*, 126:037002, Jan 2021. doi: 10.1103/PhysRevLett.126.037002.

[60] S. Arumugam, N. Môri, N. Takeshita, H. Takashima, T. Noda, H. Eisaki, and S. Uchida. Competition of static stripe and superconducting phases in $La_{1.48}Nd_{0.4}Sr_{0.12}CuO_4$ controlled by pressure. *Phys. Rev. Lett.*, 88:247001, May 2002. doi: 10.1103/PhysRevLett.88.247001.

[61] Nao Takeshita, Takao Sasagawa, Takenari Sugioka, Yoshinori Tokura, and Hidenori Takagi. Gigantic anisotropic uniaxial pressure effect on superconductivity within the CuO_2 plane of $La_{1.64}Eu_{0.2}Sr_{0.16}CuO_4$: Strain control of stripe criticality. *Journal of the Physical Society of Japan*, 73(5):1123–1126, 2004. doi: 10.1143/JPSJ.73.1123.

[62] Control of stripes/superconductivity competition in $(La,Eu,Sr)_2CuO_4$ crystals using uniaxial pressure. *Physica B: Condensed Matter*, 359-361:436 – 438, 2005. ISSN 0921-4526. doi: https://doi.org/10.1016/j.physb.2005.01.089. Proceedings of the International Conference on Strongly Correlated Electron Systems.

[63] Z. Guguchia, D. Das, C. N. Wang, T. Adachi, N. Kitajima, M. Elender, F. Brückner, S. Ghosh, V. Grinenko, T. Shiroka, M. Müller, C. Mudry, C. Baines, M. Bartkowiak, Y. Koike, A. Amato, J. M. Tranquada, H.-H. Klauss, C. W. Hicks, and H. Luetkens. Using uniaxial stress to probe the relationship between competing superconducting

states in a cuprate with spin-stripe order. *Phys. Rev. Lett.*, 125:097005, Aug 2020. doi: 10.1103/PhysRevLett.125.097005.

[64] S. Blanco-Canosa, E. Schierle, Z. W. Li, H. Guo, T. Adachi, Y. Koike, O. Sobolev, E. Weschke, A. C. Komarek, and C. Schüßler-Langeheine. Magnetic field effect in stripe-ordered 214 $(La_{1.6-x}Nd_{0.4})Sr_xCuO_4$ and $La_{2-x}Ba_xCuO_4$ superconducting cuprates studied by resonant soft x-ray scattering. *Phys. Rev. B*, 97:195130, May 2018. doi: 10.1103/PhysRevB.97.195130.

[65] T. Valla, A. V. Fedorov, Jinho Lee, J. C. Davis, and G. D. Gu. The ground state of the pseudogap in cuprate superconductors. 314(5807):1914–1916, 2006. ISSN 0036-8075. doi: 10.1126/science.1134742.

[66] doi: 10.1088/1367-2630/10/10/103016.

[67] Takashi Suzuki and Toshizo Fujita. Anomalous change in crystalline structure of $(La_{1-x}Ba_x)CuO_{4-\delta}$. *Journal of the Physical Society of Japan*, 58(6):1883–1886, 1989. doi: 10.1143/JPSJ.58.1883.

[68] J. D. Axe, A. H. Moudden, D. Hohlwein, D. E. Cox, K. M. Mohanty, A. R. Moodenbaugh, and Youwen Xu. Structural phase transformations and superconductivity in $La_{2-x}Ba_xCuO_4$. *Phys. Rev. Lett.*, 62:2751–2754, Jun 1989. doi: 10.1103/PhysRevLett.62.2751.

[69] Clifford W. Hicks, Mark E. Barber, Stephen D. Edkins, Daniel O. Brodsky, and Andrew P. Mackenzie. Piezoelectric-based apparatus for strain tuning. *Review of Scientific Instruments*, 85(6):065003, 2014. doi: 10.1063/1.4881611.

[70] Resonant ultrasound spectroscopic techniques for measurement of the elastic moduli of solids. *Physica B: Condensed Matter*, 183(1):1 – 24, 1993. ISSN 0921-4526. doi: https://doi.org/10.1016/0921-4526(93)90048-B.

[71] Frank Gugenberger, Christoph Meingast, Georg Roth, Kai Grube, Volker Breit, Thomas Weber, Helmut Wühl, S. Uchida, and Y. Nakamura. Uniaxial pressure dependence of T_c from high-resolution dilatometry of untwinned $La_{2-x}Sr_xCuO_4$ single crystals. *Phys. Rev. B*, 49:13137–13142, May 1994. doi: 10.1103/PhysRevB.49.13137.

[72] B Perea-Solano. Cryogenic Silicon Microstrip Detector Modules for LHC, 2004.

[73] A. J. Achkar, M. Zwiebler, Christopher McMahon, F. He, R. Sutarto, Isaiah Djianto, Zhihao Hao, Michel J. P. Gingras, M. Hücker, G. D. Gu, A. Revcolevschi, H. Zhang, Y.-J. Kim, J. Geck, and D. G. Hawthorn. Nematicity in stripe-ordered cuprates probed via resonant x-ray scattering. *Science*, 351(6273):576–578, 2016. doi: 10.1126/science.aad1824.

[74] H. Miao, R. Fumagalli, M. Rossi, J. Lorenzana, G. Seibold, F. Yakhou-Harris, K. Kummer, N. B. Brookes, G. D. Gu, L. Braicovich, G. Ghiringhelli, and M. P. M. Dean. Formation of incommensurate charge density waves in cuprates. *Phys. Rev. X*, 9: 031042, Sep 2019. doi: 10.1103/PhysRevX.9.031042.

[75] R. Arpaia, S. Caprara, R. Fumagalli, G. De Vecchi, Y. Y. Peng, E. Andersson, D. Betto, G. M. De Luca, N. B. Brookes, F. Lombardi, M. Salluzzo, L. Braicovich, C. Di Castro, M. Grilli, and G. Ghiringhelli. Dynamical charge density fluctuations pervading the phase diagram of a Cu-based high-T_c superconductor. *Science*, 365(6456):906–910, 2019. ISSN 0036-8075. doi: 10.1126/science.aav1315.

[76] Minoru Nohara, Takashi Suzuki, Yoshiteru Maeno, Toshizo Fujita, Isao Tanaka, and Hironao Kojima. Unconventional lattice stiffening in superconducting $La_{2-x}Sr_xCuO_4$ single crystals. *Phys. Rev. B*, 52:570–580, Jul 1995. doi: 10.1103/PhysRevB.52.570. URL https://link.aps.org/doi/10.1103/PhysRevB.52.570.

[77] Yen-Pei Fu, Adi Subardi, Min-Yen Hsieh, and Wen-Ku Chang. Electrochemical properties of $La_{0.5}Sr_{0.5}Co_{0.8}M_{0.2}O_{3-\delta}$ (M=Mn, Fe, Ni, Cu) perovskite cathodes for IT-SOFCs. *Journal of the American Ceramic Society*, 99(4):1345–1352, 2016. doi: 10.1111/jace.14127.

[78] Clifford W. Hicks, Mark E. Barber, Stephen D. Edkins, Daniel O. Brodsky, and Andrew P. Mackenzie. Piezoelectric-based apparatus for strain tuning. *Review of Scientific Instruments*, 85(6):065003, 2014. doi: 10.1063/1.4881611.

[79] Alexander Steppke, Lishan Zhao, Mark E. Barber, Thomas Scaffidi, Fabian Jerzembeck, Helge Rosner, Alexandra S. Gibbs, Yoshiteru Maeno, Steven H. Simon, Andrew P. Mackenzie, and Clifford W. Hicks. Strong peak in T_c of Sr_2RuO_4 under uniaxial pressure. *Science*, 355(6321), 2017. ISSN 0036-8075. doi: 10.1126/science.aaf9398.

[80] B. Keimer and J. E. Moore. The physics of quantum materials. *Nature Physics*, (11): 1045–1055.

[81] Bernhard Keimer, Steven A Kivelson, Michael R Norman, Shinichi Uchida, and J Zaanen. From quantum matter to high-temperature superconductivity in copper oxides. *Nature*, 518(7538):179–186, 2015.

[82] RM Fernandes, AV Chubukov, and J Schmalian. What drives nematic order in iron-based superconductors? *Nature Physics*, 10(2):97–104, 2014.

[83] Amalia I. Coldea and Matthew D. Watson. The key ingredients of the electronic structure of fese. *Annual Review of Condensed Matter Physics*, 9(1):125–146, 2018. doi: 10.1146/annurev-conmatphys-033117-054137.

[84] Alex Frano, Santiago Blanco-Canosa, Bernhard Keimer, and Robert J Birgeneau. Charge ordering in superconducting copper oxides. *Journal of Physics: Condensed Matter*, 32(37):374005, 2020.

[85] Riccardo Arpaia and Giacomo Ghiringhelli. Charge order at high temperature in cuprate superconductors. *Journal of the Physical Society of Japan*, 90(11):111005, 2021. doi: 10.7566/JPSJ.90.111005.

[86] Y. Kohsaka, C. Taylor, K. Fujita, A. Schmidt, C. Lupien, T. Hanaguri, M. Azuma, M. Takano, H. Eisaki, H. Takagi, S. Uchida, and J. C. Davis. An intrinsic bond-centered electronic glass with unidirectional domains in underdoped cuprates. *Science*, 315(5817):1380–1385, 2007. doi: 10.1126/science.1138584.

[87] Magnetism in La_2CuO_4 based compounds. *Physica C: Superconductivity*, 158(1):192 – 196, 1989. ISSN 0921-4534. doi: https://doi.org/10.1016/0921-4534(89)90316-X.

[88] Jan Zaanen and Olle Gunnarsson. Charged magnetic domain lines and the magnetism of high-T_c oxides. *Phys. Rev. B*, (10):7391, October . doi: 10.1103/PhysRevB.40.7391.

[89] S. A. Kivelson, E. Fradkin, and V. J. Emery. Electronic liquid-crystal phases of a doped Mott insulator. *Nature*, 393(6685):550–553, June 1998. ISSN 1476-4687.

[90] Bo-Xiao Zheng, Chia-Min Chung, Philippe Corboz, Georg Ehlers, Ming-Pu Qin, Reinhard M. Noack, Hao Shi, Steven R. White, Shiwei Zhang, and Garnet Kin-Lic Chan. Stripe order in the underdoped region of the two-dimensional Hubbard model. *Science*, 358(6367):1155–1160, 2017. ISSN 0036-8075. doi: 10.1126/science.aam7127.

[91] Edwin W. Huang, Christian B. Mendl, Shenxiu Liu, Steve Johnston, Hong-Chen Jiang, Brian Moritz, and Thomas P. Devereaux. Numerical evidence of fluctuating stripes in the normal state of high-T_c cuprate superconductors. *Science*, 358(6367):1161–1164, 2017. ISSN 0036-8075. doi: 10.1126/science.aak9546.

[92] F. Boschini, M. Minola, R. Sutarto, E. Schierle, M. Bluschke, S. Das, Y. Yang, M. Michiardi, Y. C. Shao, X. Feng, S. Ono, R. D. Zhong, J. A. Schneeloch, G. D. Gu, E. Weschke, F. He, Y. D. Chuang, B. Keimer, A. Damascelli, A. Frano, and E. H. da Silva Neto. Dynamic electron correlations with charge order wavelength along all directions in the copper oxide plane. *Nature Communications*, (1):597. doi: 10.1038/s41467-020-20824-7.

[93] L de'Medici and M Capone. The iron pnictide superconductors: An introduction and overview. 2017.

[94] Rong Yu, Haoyu Hu, Emilian M. Nica, Jian-Xin Zhu, and Qimiao Si. Orbital selectivity in electron correlations and superconducting pairing of iron-based superconductors. *Frontiers in Physics*, 9:92, 2021.

[95] P. O. Sprau, A. Kostin, A. Kreisel, A. E. Böhmer, V. Taufour, P. C. Canfield, S. Mukherjee, P. J. Hirschfeld, B. M. Andersen, and J. C. SÃ©amus Davis. Discovery of orbital-selective cooper pairing in fese. *Science*, 357(6346):75–80, 2017. doi: 10.1126/science.aal1575.

[96] A. Kostin, P. O. Sprau, A. Kreisel, Yi Xue Chong, A. E. Böhmer, P. C. Canfield, P. J. Hirschfeld, B. M. Andersen, and J. C. Séamus Davis. Imaging orbital-selective quasiparticles in the hund's metal state of fese. *Nature Materials*, (10):869–874. doi: 10.1038/s41563-018-0151-0.

[97] Yoshikazu Mizuguchi, Fumiaki Tomioka, Shunsuke Tsuda, Takahide Yamaguchi, and Yoshihiko Takano. Substitution effects on fese superconductor. *Journal of the Physical Society of Japan*, 78(7):074712, 2009. doi: 10.1143/JPSJ.78.074712.

[98] Suguru Hosoi, Kohei Matsuura, Kousuke Ishida, Hao Wang, Yuta Mizukami, Tatsuya Watashige, Shigeru Kasahara, Yuji Matsuda, and Takasada Shibauchi. Nematic quantum critical point without magnetism in $fese_{1-x}s_x$ superconductors. *Proceedings of the National Academy of Sciences*, 113(29):8139–8143, 2016.

[99] Amalia I. Coldea. Electronic nematic states tuned by isoelectronic substitution in bulk $fese_{1-x}s_x$. *Frontiers in Physics*, 8:528, 2021.

[100] Anna E Böhmer, Valentin Taufour, Warren E Straszheim, Thomas Wolf, and Paul C Canfield. Variation of transition temperatures and residual resistivity ratio in vapor-grown fese. *Physical Review B*, 94(2):024526, 2016.

[101] S. A. Moore, J. L. Curtis, C. Di Giorgio, E. Lechner, M. Abdel-Hafiez, O. S. Volkova, A. N. Vasiliev, D. A. Chareev, G. Karapetrov, and M. Iavarone. Evolution of the superconducting properties in $fese_{1-x}s_x$. *Phys. Rev. B*, 92:235113, Dec 2015. doi: 10.1103/PhysRevB.92.235113.

[102] Tetsuo Hanaguri, Katsuya Iwaya, Yuhki Kohsaka, Tadashi Machida, Tatsuya Watashige, Shigeru Kasahara, Takasada Shibauchi, and Yuji Matsuda. Two distinct superconducting pairing states divided by the nematic end point in $fese_{1-x}s_x$. *Science Advances*, 4(5):eaar6419, 2018. doi: 10.1126/sciadv.aar6419.

[103] C. J. Arguello, E. P. Rosenthal, E. F. Andrade, W. Jin, P. C. Yeh, N. Zaki, S. Jia, R. J. Cava, R. M. Fernandes, A. J. Millis, T. Valla, R. M. Osgood, and A. N. Pasupathy. Quasiparticle interference, quasiparticle interactions, and the origin of the charge density wave in $2h-nbse_2$. *Phys. Rev. Lett.*, 114:037001, Jan 2015. doi: 10.1103/PhysRevLett.114.037001.

[104] Eduardo H. da Silva Neto, Pegor Aynajian, Alex Frano, Riccardo Comin, Enrico Schierle, Eugen Weschke, András Gyenis, Jinsheng Wen, John Schneeloch, Zhijun Xu,

Shimpei Ono, Genda Gu, Mathieu Le Tacon, and Ali Yazdani. Ubiquitous interplay between charge ordering and high-temperature superconductivity in cuprates. *Science*, (6169):393–396. doi: 10.1126/science.1243479.

[105] Luke C. Rhodes, Jakob Böker, Marvin A. Müller, Matthias Eschrig, and Ilya M. Eremin. Non-local d_{xy} nematicity and the missing electron pocket in fese. *npj Quantum Materials*, 6(1):45, May 2021. ISSN 2397-4648. doi: 10.1038/s41535-021-00341-6.

[106] Vladimir Cvetkovic and Oskar Vafek. Space group symmetry, spin-orbit coupling, and the low-energy effective hamiltonian for iron-based superconductors. *Phys. Rev. B*, 88: 134510, Oct 2013. doi: 10.1103/PhysRevB.88.134510.

[107] Chi Ming Yim, Christopher Trainer, Ramakrishna Aluru, Shun Chi, Walter N Hardy, Ruixing Liang, Doug Bonn, and Peter Wahl. Discovery of a strain-stabilised smectic electronic order in lifeas. *Nature communications*, 9(1):1–7, 2018.

[108] Wei Li, Yan Zhang, Peng Deng, Zhilin Xu, S-K Mo, Ming Yi, Hao Ding, M Hashimoto, RG Moore, D-H Lu, et al. Stripes developed at the strong limit of nematicity in fese film. *Nature Physics*, 13(10):957–961, 2017.

[109] Yonghao Yuan, Xuemin Fan, Xintong Wang, Ke He, Yan Zhang, Qi-Kun Xue, and Wei Li. Incommensurate smectic phase in close proximity to the high-t_c superconductor fese/srtio$_3$. *Nature Communications*, 12(1):1–9, 2021.

[110] S. Chibani, D. Farina, P. Massat, M. Cazayous, A. Sacuto, T. Urata, Y. Tanabe, K. Tanigaki, A. E. Böhmer, P. C. Canfield, M. Merz, S. Karlsson, P. Strobel, P. Toulemonde, I. Paul, and Y. Gallais. Lattice-shifted nematic quantum critical point in fese$_{1-x}$s$_x$. *npj Quantum Materials*, (1):37. doi: 10.1038/s41535-021-00336-3.

[111] Weilu Zhang, Shangfei Wu, Shigeru Kasahara, Takasada Shibauchi, Yuji Matsuda, and Girsh Blumberg. Quadrupolar charge dynamics in the nonmagnetic $FeSe_{1-x}S_x$ superconductors. *Proceedings of the National Academy of Sciences*, 118(20), 2021.

[112] Amalia I. Coldea, Samuel F. Blake, Shigeru Kasahara, Amir A. Haghighirad, Matthew D. Watson, William Knafo, Eun Sang Choi, Alix McCollam, Pascal Reiss, Takuya Yamashita, Mara Bruma, Susannah C. Speller, Yuji Matsuda, Thomas Wolf, Takasada Shibauchi, and Andrew J. Schofield. Evolution of the low-temperature fermi surface of superconducting fese$_{1-x}$s$_x$ across a nematic phase transition. *npj Quantum Materials*, (1):2.

[113] L. Gannon, A. Bosak, R. G. Burkovsky, G. Nisbet, A. P. Petrović, and M. Hoesch. A device for the application of uniaxial strain to single crystal samples for use in synchrotron radiation experiments. *Review of Scientific Instruments*, 86(10):103904, 2015. doi: 10.1063/1.4933383.

Appendix A

Piezoelectric Strain Device

The design for the strain device was inspired by an original design conceived by Hicks et al [78]. A schematic overiew of the apparatus is shown in Fig. A.1(a).It features three piezo stack actuators which supply the strain and a movable sample plate to allow for adjustments of the sample space. The principles of operation are as follows: negative (compressive) strain is acheived by applying a positive voltage to the middle stack and negative voltages to the outer stack and positive (tensile) strain is by applying the voltages vice versa (see Fig. A.1(b)).

The use of three piezo adjacent stacks mitigates the effects of thermal expansion of the piezos upon cooling, which can be significant. Also, the frame is constructed of titanium since it possesses a relatively small thermal expansion coefficient. These considerations paired with UHV/cryogenic compatible piezo stacks allows for operation at low temperatures. The stroke of piezoelectric stacks, however, is suppressed at lower temperatures, with one group citing a decrease by a factor of 4 from room temperature to 4 K [113]. Another favorable aspect of this design is that the device is thin in the direction perpendicular to the sample, which will be discussed in describing the diffractometer.

The device that I constructed, shown in Fig. A.1(c), is a smaller adaptation of the apparatus designed by Hicks et al. Similar features include the use of three piezo stacks,

titanium as the frame material, and a slotted sample holder to allow for adjustments of the sample gap size. The stacks are APC Pst 150 cryo/UHV coated actuators with a 2 x 3 mm cross section. Various sizes of stacks were used for the devices, ranging from 5 mm to 20 mm, to provide options for the amount of strain and overall size of the device. The overall dimensions of the smallest device are shown in Fig. A.1a.

The U-frame contains through holes fitted for M2 screws used to mount the device inside of the diffractometer. Four "pins" of 0.20 CDA 101 copper wire from the California Fine Wire Company are situated at the corners of the U-frame. The pins serve as electrical contacts for the piezo stacks (see Fig A.1(c)) and are fit into sapphire tubes to provide insulation from the frame. T lead (red) wire of each piezo is soldered with lead-free solder to its own pin, while all three ground (white) wires are soldered to a single pin. Copper collets fit onto the ends of the pins and provide ease in making electrical connections to external electronic devices 0.1 mm slots were made on the top of the back frame to aid in the alignment of the piezos. The frame pieces are slightly oversized (+0.2 mm on each side relative to the cross section of the stacks) to allow for slight misalignments during construction. The rectangular pieces that define the sample gap are secured to the device by M1.2 screws. The top sample holder fits into a U-frame and contains a slot to allow for adjustment of the sample gap size, while the bottom sample holder is secured to the central piezo. EPO-TEK® H74f epoxy was used to glue the piezo stacks to the frame components and mount the samples onto the device. This specific epoxy was chosen because of its hardness (important for applying strain) and reliability in cryogenic/UHV environments.

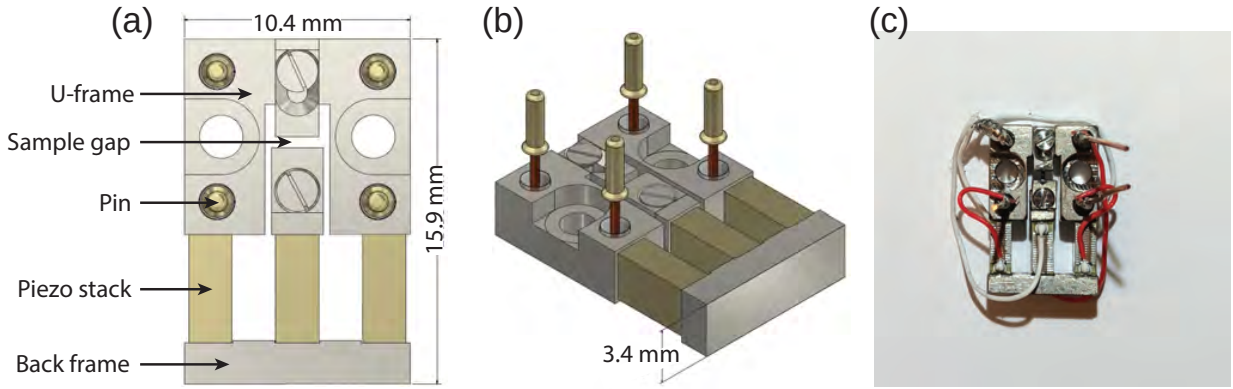

Figure A.1: Piezoelectric Strain Device: (**a**) A schematic of the device showing the in-plane dimensions. (**b**) An isometric view of the device showing the thickness and orientation of the pins. (**c**) An image of the device itself.

Appendix B

X-ray scattering geometry

A typical RXS endstation, shown schematically in Figure B.1(a), contains a diffractometer with several translational and rotational degrees of freedom including the (x, y, z) position of the sample, the angle of the sample's surface and the incoming beam, θ, and the azimuthal angle of the sample. By adjusting these parameters, along with the photon energy and position of the detector, 2θ, periodic structures of electrons can be measured.

The diffraction process can be understood from Bragg's law, which predicts constructive interference between incoming and outgoing rays when the path-length difference between rays is equal to an integer value of the wavelength. This is depicted in Figure B.1(b) and can be expressed mathematically as

$$A + B = 2d \sin(\theta_B) = n\lambda. \tag{B.1}$$

Following this equation, we can observe peaks by adjusting the angle of incidence, θ, or the wavelength of light, λ, to fulfill the Bragg condition. We can also approach this problem

in reciprocal space and treat the incoming and outgoing rays as plane waves with wavevectors $\boldsymbol{k}$ and $\boldsymbol{k}$' respectively, where

$$\boldsymbol{k} = |\boldsymbol{k}|\,\boldsymbol{n} \tag{B.2}$$

$$\boldsymbol{k}' = |\boldsymbol{k}|\,\boldsymbol{n}' \tag{B.3}$$

$$|\boldsymbol{k}| = \frac{2\pi}{\lambda}. \tag{B.4}$$

The rays reflect off of two reciprocal lattice points and the path length difference is

$$A + B = \boldsymbol{d} \cdot (\boldsymbol{n} - \boldsymbol{n}') = \frac{\lambda}{2\pi}\boldsymbol{d} \cdot (\boldsymbol{k} - \boldsymbol{k}') = n\lambda, \tag{B.5}$$

as shown in Figure B.1(c). We can define the momentum transfer vector, $\boldsymbol{Q} = (\boldsymbol{k} - \boldsymbol{k}')$, and equation B.5 becomes

$$\boldsymbol{d} \cdot \boldsymbol{Q} = 2\pi n \tag{B.6}$$

This formula is known as the Laue condition, and is the reciprocal-space vector equivalent of Bragg's law. Simply put, this formula states that constructive interference occurs when the momentum transfer vector is equal to a reciprocal space lattice vector. However, in general, $\boldsymbol{Q}$ can be any vector in reciprocal space that is physically allowed. For an orthorhombic lattice, a reciprocal space vector can be expressed in terms of the Miller indices (h, k, l) and the lattice constants (a, b, c) as

$$\boldsymbol{Q} = 2\pi\sqrt{\frac{h^2}{a^2} + \frac{k^2}{b^2} + \frac{l^2}{c^2}} \tag{B.7}$$

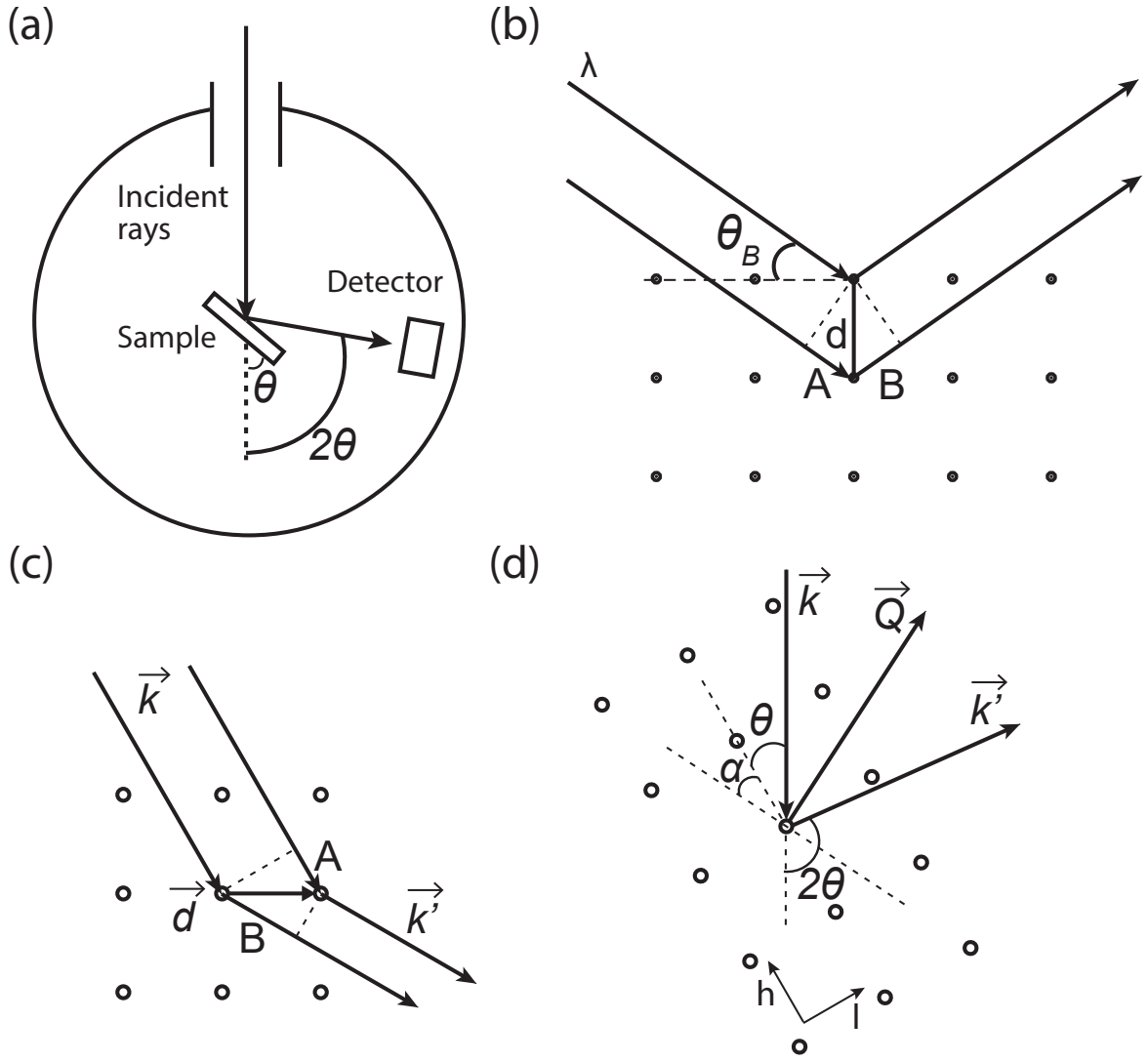

Figure B.1: Scattering Geometry: (**a**) Schematic of a typical RXS endstation. θ and 2θ represent the angles of the sample and detector relative to the incident rays. **b**) Scattering diagram depicting Bragg's law in real-space. The light is incident from the left with a wavelength of λ at an angle of θ_B relative to the plane of the lattice. d is the atomic spacing, and A+B is the path length difference between rays that reflect off of consecutive layers. (**c**) Scattering diagram depicting the Laue condition in reciprocal space. (**d**) Diagram showing the connection between the scattering diagram and the Miller indices. The sample angle, detector angle and photon energy are chosen to probe a specific plane, $Q = (h, l)$, at an angle, α, to in-plane direction of the crystal.

In x-ray scattering experiments, we change the orientation of the sample, the angle of reflection, and the photon energy to probe specific points in reciprocal space. To make this equation more useful in practice, we want to rewrite it in terms of the parameters that we control, namely the angle of the sample, θ, the angle of the detector, 2θ, and the photon energy, E. To do this we will consider a square reciprocal lattice at an angle θ and a detector at an angle 2θ, both relative to the direction of the incoming beam, $\boldsymbol{n}$ (see Figure B.1(d)). For simplicity, we will ignore the sample flip direction and treat the problem two dimensionally in the h-l plane.

We can apply Bragg's law (equation B.1), where

$$\theta_B = \theta + \alpha = \theta - \arctan\left(\frac{hc}{la}\right), \text{and} \tag{B.8}$$

$$|\boldsymbol{d}| = \frac{2\pi}{|\boldsymbol{Q}|} = \left(\frac{h^2}{a^2} + \frac{l^2}{c^2}\right)^{-\frac{1}{2}}, \tag{B.9}$$

resulting in

$$\theta = \arcsin\left(\frac{1240\,\text{eV nm}}{4\pi\,E}\left(\frac{h^2}{a^2} + \frac{l^2}{c^2}\right)^{-\frac{1}{2}}\right) + \arctan\left(\frac{hc}{la}\right), \text{and} \tag{B.10}$$

$$2\theta = 2\arcsin\left(\frac{1240\,\text{eV nm}}{4\pi\,E}\left(\frac{h^2}{a^2} + \frac{l^2}{c^2}\right)^{-\frac{1}{2}}\right) \tag{B.11}$$

Using these equations, one can calculate the θ and 2θ positions provided the photon energy and Miller indices of interest. Additionally, these equations can be rewritten in terms of the lattice constants, a and c, allowing you to determine the lattice parameters given the positions of a Bragg peak.